Analytical Expressions of Radiocarbon Distribution in Transient State Unconfined Aquifers and Their Application to Determination of Past and Present Recharges of North Africa Aquifers

Amine Chekireb, Julio Gonçalvès, Bruno Hamelin, Pierre Deschamps, Séraphin Pierre

AGU ADVANCING EARTH AND SPACE SCIENCE

Water Resources Research

RESEARCH ARTICLE
10.1029/2021WR030018

Analytical Expressions of Radiocarbon Distribution in Transient State Unconfined Aquifers and Their Application to Determination of Past and Present Recharges of North Africa Aquifers

Amine Chekireb[1], Julio Gonçalvès[1], Bruno Hamelin[1], Pierre Deschamps[1], and Pierre Séraphin[1]

[1]Aix Marseille University, CNRS, IRD, INRAE, Coll France, CEREGE, Aix-en-Provence, France

Key Points:

- Analytical expressions for Radiocarbon distribution in transient state and unconfined aquifers
- Determination of recharge rates of North Africa aquifers by using radiocarbon tracers accounting for past climate variability
- The use of Vogel's standard solution for North Africa aquifers leads to an average overestimation of present-day recharge of about 70%

Correspondence to:
A. Chekireb,
chekireb@cerege.fr and
amine.chekireb@gmail.com

Citation:
Chekireb, A., Gonçalvès, J., Hamelin, B., Deschamps, P., & Séraphin, P. (2021). Analytical expressions of radiocarbon distribution in transient state unconfined aquifers and their application to determination of past and present recharges of North Africa aquifers. *Water Resources Research*, *57*, e2021WR030018. https://doi.org/10.1029/2021WR030018

Received 25 MAR 2021
Accepted 17 OCT 2021

Abstract In this study, we developed two-dimensional hydrodynamic age expressions for the free-surface aquifer problem required for radiocarbon data interpretation in terms of recharge. Time-varying recharge is accounted for in fully transient or pseudo-steady state alternative analytical expressions applying to weakly or highly hydraulically reactive unconfined aquifers, respectively. These expressions extend the well-known model proposed by Vogel in 1967 and represent a convenient alternative approach to the more complex numerical solution of a particle tracking problem considering climate variability. An application of the developed expressions was carried out to assess past (40 Kyr) and present recharge rates for the North Western Sahara Aquifer System (NWSAS) and the Djeffara plain (Tunisia-Libya). Using the available ^{14}C data at different outcrops, we obtained local recharge values ranging from 0.2 ± 1.7 to 4.5 ± 3.2 mm yr^{-1}. Here, it is shown that using the standard purely steady-state model for radiocarbon interpretation leads to a present recharge overestimation of up to 360%. A linear relation between the present recharge and the average annual rainfall was obtained and used to identify the regional distribution of the recharge and domain-averaged values. Global values of 1.6 ± 2.3 mm yr^{-1} for the NWSAS and 3.5 ± 2.3 mm yr^{-1} for the Djeffara are in excellent agreement with the values obtained by hydrogeological models and derived using Satellite gravity data. The relation between recharge and rainfall obtained here can be used as a first-order estimate for hydrogeological modeling or water management analysis for aquifers in the Saharan area.

1. Introduction

Determining groundwater recharge is fundamental for the understanding and management of groundwater systems, especially for renewability analysis. Assessing the long-term recharge rate is pivotal to understand aquifers' behavior and predict potential effects of recent climate and land use changes on groundwater resources. Recharge rate can be defined as the amount of water that effectively flows across the unsaturated zone and reaches the water table of an aquifer over a given time. Among the different methods to identify the recharge, such as numerical modeling (unsaturated or saturated zone) and water table fluctuation, the use of geochemical tracers is one of the most appropriate approaches especially in arid environments where recharge is low and sporadic (Cartwright et al., 2017; Cook et al., 1992; Scanlon, 2000; Scanlon et al., 2002, 2006). In such environments, recharge occurs according to two mechanisms: diffuse recharge by direct infiltration of precipitation and focused recharge by infiltration of wadi floods (Scanlon et al., 2006). Moreover, in the most arid areas, uptake of groundwater at the water table by evaporation was quantitatively identified by Fontes et al. (1986) who termed this flux a diffuse discharge which therefore corresponds to a "negative net recharge" (i.e., when evaporation exceeds recharge; Lekula & Lubczynski, 2019). This evaporation groundwater uptake was recently modeled (Kamai & Assouline, 2018; Lekula & Lubczynski, 2019) and measured in situ (Schulz et al., 2015). Beside the chloride mass balance approach, the most commonly used tracers are radioactive isotopes, such as ^{36}Cl, ^{14}C, or ^{3}H (e.g., Abid et al., 2012; Cartwright et al., 2017; Clark & Fritz, 1997; Cook et al., 1994; Guendouz et al., 2003; Le Gal la Salle et al., 2001; Newman et al., 2010; Petersen, 2014; Scanlon, 2000; Tweed et al., 2011). Making use of the radioactive decay of such isotopes, groundwater ages (i.e., travel time of a fluid particle from its entry into the water table to its current position) and velocities in confined and unconfined aquifers can be estimated, which enables recharge

rates to be determined. This approach was used in several studies to determine travel time distributions (Cartwright et al., 2020; Cook & Böhlke, 2000; Gerber et al., 2018; Samborska et al., 2013) and to investigate either the existence or the magnitude of the recharge (e.g., Böhlke, 2002; Bredenkamp & Vogel, 1970; Delin et al., 2000, 2007; Edmunds & Wright, 1979; Leaney & Allison, 1986; McMahon et al., 2011; Verhagen, 1992). Groundwater ages derived from radioactive isotopes interpreted in terms of recharge rates can be simply estimated using a hydrodynamic age model as proposed by Vogel (1967). This model is based on a particle tracking approach consisting in parametric equations giving the (x, z) location of a fluid particle at any given time for a simplified unconfined aquifer of constant thickness and porosity receiving a constant recharge in time and space. Vogel's (1967) model provides a vertical distribution of theoretical ages (or radioisotope concentrations) corresponding to vertically stratified streamflow lines carrying different concentrations and underlying groundwater ages and allows a straightforward data interpretation. Moreover, this parsimonious approach represents a simple alternative method to more complex, time- and cpu-consuming fluid flow, and reactive transport models (e.g., Cartwright et al., 2020; Sanford, 2002) to directly interpret radioisotope concentrations. Building such complex models may even be impossible due to data scarcity (geometry, permeability, storativity, and hydraulic heads). The approach based on Vogel's model was used for recharge estimation in various studies (e.g., Delin et al., 2000, 2007; Harrington et al., 2002; McCallum et al., 2020; McMahon et al., 2011).

Vogel's approach applies to a vertical profile of radioisotope concentrations in an unconfined aquifer, which is generally not available unless the data are obtained using nested wells (multi-level). For the most common situation of well screening over the entire water column, the interpretation of the data using Vogel's model depends on the sampling method. If the sampling method does not disturb the stratification (i.e., low pumping rate in a chamber limited by packers), the model can be directly used by implementing the sampling depth. Conversely, when it comes to installations presenting high pumping rates (e.g., those used for water supply) for moderate to deep sampling, the sampling likely yields a mixing of vertically stratified streamlines, especially if the pump is located in the middle of the screened interval depth (Lasagna & De Luca, 2016; Leray et al., 2012; Wood et al., 2017; Zinn & Konikow, 2007). In the event of mixing, due to the non-linearity of the groundwater age model (exponential decay), the age that could be calculated using the average radioisotope activity does not correspond to the mean age of the individual streamlines carrying different radioactive isotope activities. This well-known bias associated to heavy pumping (converging flow lines) is referred to by introducing the notion of apparent age (Bethke & Johnson, 2008) and was discussed as a drawback for all environmental tracers by McCallum et al. (2015) and specifically for radiocarbon approaches by Cartwright et al. (2020). In both cases, a model for the radioactive isotope vertical distribution of an unconfined aquifer is needed to accurately interpret the sampled concentrations.

Moreover, a fundamental drawback when interpreting data using Vogel's model is the assumption of a constant recharge. Indeed, for regional-scale and thick aquifers with long residence times for which radiocarbon is often used, the recharge is largely affected by recent Quaternary climate fluctuations. In the circum-Sahara area, besides the glacial (presumably dry) and interglacial (wet) alternations (see, e.g., Petersen, 2014), a more humid period (African Humid Period, AHP) between −10 and −5 ka was highlighted by several marine or continental records (Collins et al., 2017; deMenocal et al., 2000; Gasse, 2000; Tierney et al., 2017). These climatic fluctuations impact the past recharge of regional-scale aquifers as recorded in groundwater by isotopic tracers (radiocarbon and stable isotopes of hydrogen and oxygen; Edmunds et al., 2003). Hence, the relevance of using Vogel's model based on the assumption of a constant recharge for the ^{14}C data interpretation of systems characterized by time constants of several tens of thousands of years is questionable. An answer would be that the interpretation using Vogel's model yields a recharge value averaging the temporal resolution of the radioisotope (e.g., Wood et al., 2015). However, for current management purposes, the present-day recharge value must be preferentially ascertained.

Accounting for Quaternary climate variability, and therefore recharge temporal variations, generally imposes the use of (numerical) models that are much more complex than Vogel's model (e.g., Petersen, 2014; Schulz et al., 2017). In a simpler approach, the validity of the Vogel expressions can however be extended to take into account the temporal variation of the recharge. In that respect, McCallum et al. (2020) recently proposed an analytical approach based on Vogel's expression to assess the effects of recharge variation over the few last decades. The authors associated a slightly modified Vogel model with the stretching method

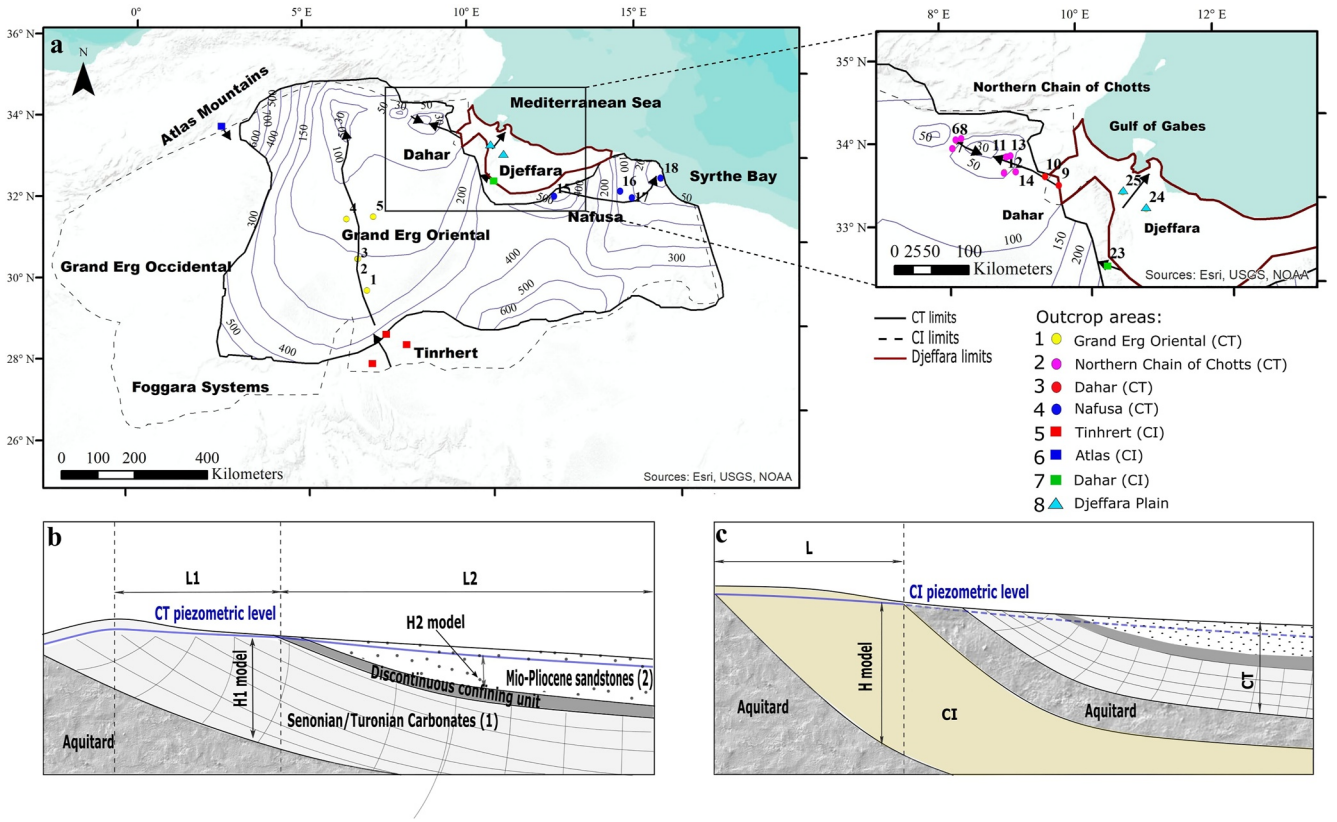

Figure 1. (a) Location map showing the extent of the Complex Terminal (CT), the Continental Intercalaire (CI), and the Djeffara aquifers and the location of the samples. (b and c) Schematic views of the hydrogeological contexts of the sampling sites.

of Massoudieh (2013) to extend the flowlines beyond a vertical boundary in order to calculate ^{14}C and age distributions on a horizontal discharge zone using a pseudo-steady state (instantaneous velocity changes) assumption. Here, by introducing more in-depth alterations to Vogel's model than McCallum et al. (2020), we show the possibility of extending Vogel's analytical approach to more realistic transient systems subject to time-varying recharge rates.

The new expressions are used to interpret the radiocarbon activity of samples collected in wells with large pumping rate facilities leading to a vertical mixing which is a common situation. Following a presentation of the application domain and the available radiocarbon data, we describe the new conceptualization of Vogel's model introducing the temporal variation of recharge, by analyzing the hydrodynamics applying to a 2D free-surface aquifer. Two sets of expressions were developed to adapt to differences in aquifer reactivity: fully transient state (TS) and pseudo steady state (PSS) models. These expressions are then applied to assess the recharge rates for the North Western Sahara Aquifer System (NWSAS) and the Djeffara plain aquifer (Tunisia and Lybia; Figure 1). For this purpose, the available ^{14}C data are interpreted by accounting for the climate variability given by the most recent climate reconstructions for northwestern Africa (e.g., Collins et al., 2017; Pausata et al., 2020).

2. Hydrological and Climatic Context of North Africa Aquifers and Available Radiocarbon Data

2.1. Hydrological Systems

2.1.1. North Western Sahara Aquifer System

Extending over about 10^6 km^2 (Algeria, Tunisia, and Libya; Figure 1), NWSAS is characterized by depths up to 3,000 m and is one of the largest transboundary aquifers in the world (MacDonald et al., 2012). This

multilayered aquifer system is mostly made of Triassic to Quaternary continental formations which contain two main hydrogeological units: the "Continental Intercalaire" (CI) and the "Complexe Terminal" (CT). The CI is a deep and mostly confined aquifer composed of middle Jurassic to lower Cretaceous formations with an average thickness of 358 m (Baba Sy, 2005). Two formations in the CI present particularly efficient aquifer properties: the Barremian and the Albian sandstone formations. These formations are separated (discontinuously at large scale but effectively at lower scale) by dolomite and clays of the Aptian. Recharge occurs at the outcrops of this regional-scale aquifer representing about 200,000 km^2 (20% of the total surface area of the CI), of which the Atlas area contributes about 70% (Gonçalvès et al., 2020). The most recent value of overall recharge for the CI was estimated at 9.4 $m^3 s^{-1}$ by hydrogeological modeling (Baba Sy, 2005). The CT aquifer is a multi-layer aquifer which comprises two interconnected formations separated by discontinuous shaly to marly confining units: Mio-Pliocene sands and upper Cretaceous and Eocene carbonates (Figure 1b). Due to the discontinuity of these confining units between the two aquifer formations, the CT is considered a single aquifer at regional scale. However, at local scale (well tests), the hydraulic effects of the confining unit cannot be omitted. The CT aquifer has an average thickness of 340 m (average saturated thickness 250 m) and extends over 660,000 km^2. Its main outcropping areas are the Algerian and Tunisian Chotts in the north, the eastern flank of Dahar and Jabal Nafusa in the east, the plateau of Tinrhert and Tademaït in the south, and the M'zab dorsal in the west (Baba Sy, 2005; Guendouz et al., 2003; Observatoire du Sahara et du Sahel [OSS], 2002). The main recharge area of the shallow and mostly unconfined CT is located in the Central Sahara. The most recent global recharge estimates were estimated at 18.2 $m^3 s^{-1}$ by hydrogeological modeling (Baba Sy, 2005; OSS, 2003; Zammouri & Ribeiro, 2017).

2.1.2. Djeffara Plain Aquifer

The northern part of the Djeffara plain is one of the main discharge areas for CI groundwater (see, e.g., Gonçalvès et al., 2015). In the Gabès region (Tunisia; Figure 1), the thinning of the CI and a northwestward increase in clay content reducing the aquifer transmissivity cause upward CI groundwater circulation through the El-Hamma fault network. The Djeffara sedimentary plain contains a shallower multi-layer aquifer, formed by Miocene continental deposits (clays intercalated with conglomeratic and sandy layers), Senonian limestones, Turonian carbonates (dolomites and limestones), and Triassic sandstones. The groundwater flow is generally directed toward the shoreline. Due to mixing processes between old waters from the CI and local recharge, which was observed based on the piezometric map, the north Djeffara plain was excluded from the present study. Conversely, in the southern part of the Djeffara plain, the free-surface outcrops of the Jurassic and Triassic aquifers receive a local recharge (OSS, 2006).

2.2. Present and Past Climatic Context

The northern fringe of the NWSAS and the Djeffara plain are characterized by a seasonal Mediterranean climate with a rainy winter (October–March) and a dry summer (Nicholson, 2000). A large latitudinal variation in annual rainfall is observed from about 350 mm on the Atlas Mountains area to <10 mm in the southern Sahara (Baba Sy, 2005; OSS, 2003). The domain averaged value of the Average Annual Rainfall (AAR) is 70 mm yr^{-1} for the NWSAS and 190 mm yr^{-1} for the Djeffara, using the global rainfall rates at a resolution of 1° × 1° since 1901 from the CRU Climatic Research Unit (http://wps-web1.ceda.ac.uk).

The interpretation of the available ^{14}C data requires considering the climate variations of North Africa over the last 40 Kyr which corresponds to the time-period over which radiocarbon indicates groundwater flow and recharge. The climate variability during the Quaternary in the Mediterranean region and Sahara-Sahel belt has been largely studied, especially during the last glacial-interglacial alternation and the Holocene (see review in Abrantes et al., 2012; Gasse, 2000; Hoelzmann et al., 2004; Pausata et al., 2020). The coastal regions of northern Africa up to the Sahara lies at a critical boundary position between polar and subtropical air masses.

Climate variability over the Sahara is controlled by the orbitally-induced shift of the ITCZ (Intertropical Convergence Zone) and northward penetration of the monsoon rains into North Africa. During the last humid period, between ~−10 and −5 ka, referred to as the AHP, marine records (Skonieczny et al., 2015; Tierney et al., 2017) showed that monsoonal moisture reached up to 31°N latitude (i.e., the southern part of the NWSAS) in agreement with most recent modeling effort (Pausata et al., 2016). The present-day Sahara

Desert transitioned to a vegetated state (Hopcroft et al., 2017; Peyron et al., 2006) well-documented in continental archives (Gasse, 2000; Hoelzmann et al., 2004). These wetter conditions leaded to the formation of surface water bodies in the northern Sahara (Fontes et al., 1985; Lécuyer et al., 2016) and likely caused an active recharge of the Saharan aquifers (e.g., Lézine et al., 2011). Although the timing and abruptness of AHP termination are still debated, climate condition became drier during the mid-to late Holocene period (−5 ka to today; Lézine et al., 2011; Shanahan et al., 2015). The glacial period preceding the AHP is only documented by marine sediments records (notably, leaf wax isotopes δD_{wax}) that indicate dry conditions over the Northern Sahara (including the NWSAS area) during the −40 to −10 ka period (Skonieczny et al., 2015; Tierney et al., 2017; Tjallingii et al., 2008) leading to relatively low rainfall and thus low recharge.

The hydroclimate of the southern Mediterranean coast is mainly influenced by westerly precipitation and the position and strength of the wintertime North Atlantic storm tracks. Past humid periods in this region correspond to enhanced advection of Atlantic moisture with admixture along the storm track of water evaporated from Western Mediterranean Sea (Hoelzmann et al., 2004; Rogerson et al., 2019). There are multiple lines of evidence that the Western African monsoon never reached the Mediterranean realm (Tzedakis, 2007), but several studies support also precessional forcing of the Mediterranean climate, and coeval humid conditions in southern Mediterranean with maximum monsoon activity (Blanchet et al., 2021; Hoffmann et al., 2016; Kutzbach et al., 2014). During the early Holocene, substantially wetter conditions prevailed over much of southern rim of Mediterranean Sea, as documented by recent paleohydrological records (Blanchet et al., 2021; Combourieu Nebout et al., 2009; Desprat et al., 2013).

2.3. Radiocarbon Data

2.3.1. Available Radiocarbon Data

Many studies have provided ^{14}C data on groundwater in the two aquifer systems investigated here (see below). However, for the specific objectives of the present study (i.e., thorough interpretation of ^{14}C data using a simple particle tracking approach for free surface aquifers), we sorted out existing radiocarbon data according to three criteria:

1. *Geological consistency*: the multi-layer aquifers considered here are characterized by permeable formations separated by discontinuous confining layers, possibly leading to local semi-confined behavior (Figure 1b). Therefore, we consider here only radiocarbon data collected within the same geological formation showing a free-surface and for a given streamline interpretation: Mio-Pliocene sandstones or carbonate Senonian to Turonian formation for the CT, Barremian, or Albian sandstones for the CI.
2. *A clear hydrogeological context*: either a fully unconfined aquifer within a unique formation or the free-surface outcrop of a large regional scale confined aquifer (Figures 1b and 1c, respectively). This latter favorable situation enables a straightforward ^{14}C interpretation given probable small response times to the changes in recharge associated with the small length scale of the outcropping area (see Section 3).
3. *Favorable hydrodynamic context*: we selected locations characterized by diverging (or not converging) streamlines to avoid the mixing problem and discarded the outcrops corresponding to large regional streamlines of confined systems outflowing and mixing with local recharge (e.g., the Foggara region in southern Algeria, which was the main sampling area of Gonfiantini et al., 1974 for the CI).

Out of the 184 radiocarbon data published on the NWSAS and Djeffara Aquifer (Gonfiantini et al., 1974; Guendouz et al., 2003; Hadj Ammar, 2016; Hadj Ammar et al., 2014, 2020; OSS, 2003; Petersen et al., 2018; Srdoč et al., 1982; Zouari et al., 2011), only 25 were retained according to our selection criteria (see location of the samples in Figure 1 and Table 1).

2.3.2. Correction of Radiocarbon Data for Atmospheric Contamination

All the samples were obtained using large pumping facilities which yields a mixing of vertically stratified streamlines. Most of these samples were collected and analyzed using the historical method based on the extraction of the dissolved inorganic carbon by precipitation of barium or strontium carbonate from a large groundwater volume (>50 L) in the field. In this method, the carbonate precipitation is initiated by adding sodium hydroxide that made the solution hyperalkaline. As pointed out by Aggarwal et al. (2014), this method may lead to contamination of the samples by atmospheric carbon, as hyperalkaline solution

Table 1
Collected Data and Calculated Parameters for NWSAS (CT and CI) and the Djeffara Plain

Recharge zone	Sample	References	Aquifer	$A_{uncorrected}$ (pmc)	$A_{corrected}$ (pmc)	$\delta^{13}C$ (‰)	$\delta^{13}Cg$ (‰)	PH
Grand Erg Oriental CT	1	Guendouz et al., 2003	Mio-Pliocene sandstones	42.5 ± 0.8	37.65 ± 5.19	−6.60	−15	7.71
	2		Mio-Pliocene sandstones	38.9 ± 1	33.74 ± 5.11	−9.00	−15	7.54
	3		Mio-Pliocene sandstones	28 ± 3.7	21.92 ± 4.93	−6.56	−15	7.04
	4		Mio-Pliocene sandstones	24.7 ± 0.8	18.34 ± 4.91	−7.00	−15	6.66
	5		Mio-Pliocene sandstones	31.4 ± 2	25.61 ± 4.97	−9.50	−15	7.15
Northern Chain of Chotts CT	6	Hadj Ammar, 2016; Hadj Ammar et al., 2014, 2020	Mio-Pliocene sandstones	11.5 ± 1	4.03 ± 4.94	−5.72	−20	7.17
	7		Mio-Pliocene sandstones	18.3 ± 1	11.40 ± 4.90	−8.29	−20	8.10
	8		Mio-Pliocene sandstones	17.8 ± 1	10.86 ± 4.90	−6.14	−20	7.20
Dahar CT	9	Hadj Ammar, 2016; Hadj Ammar et al., 2014, 2020	Senonian carbonates	30.2 ± 1	24.31 ± 4.96	−7.32	−20	7.40
	10		Senonian carbonates	17.9 ± 1	10.97 ± 4.90	−4.18	−20	8.28
	11	Hadj Ammar, 2016; Hadj Ammar et al., 2014, 2020	Mio-Pliocene sandstones	11.2 ± 1	3.70 ± 4.95	−4.49	−20	7.30
	12		Mio-Pliocene sandstones	12.3 ± 1	4.90 ± 4.93	−5.22	−20	8.05
	13		Mio-Pliocene sandstones	12.2 ± 1	4.79 ± 4.93	−6.21	−20	7.78
	14		Mio-Pliocene sandstones	10.8 ± 1	3.27 ± 4.95	−5.22	−20	7.90
Nafusa CT	15	Srdoč et al., 1982	Turonian carbonates	9.4 ± 0.5	1.75 ± 4.97	−4.80	−20	NA
	16		Senonian carbonates	12.8 ± 0.5	5.44 ± 4.93	−3.80	−20	NA
	17		Senonian carbonates	23 ± 0.6	16.50 ± 4.90	−6.90	−20	NA
	18	OSS, 2003	Miocene sandstones	18.6 ± 1.9	11.73 ± 4.90	−4.30	−20	NA
Tinhrert CI	19	Gonfiantini et al., 1974	Albian sandstones	22.8 ± 0.8	16.28 ± 4.90	−7.20	−15	7.30
	20		Albian sandstones	17.3 ± 0.7	10.32 ± 4.90	−10.50	−15	7.60
	21		Albian sandstones	9.9 ± 1.5	2.29 ± 4.96	−10.9	−15	7.60
Atlas CI	22	Gonfiantini et al., 1974; Petersen et al., 2018	Albian sandstones	54.7 ± 1.3	50.88 ± 5.58	−7.40	−20	7.40
Dahar CI	23		Albian sandstones	42.24 ± 0.21	42.24 ± 0.21	−7.67	−20	NA
Djeffara	24	Zouari et al., 2011	Triassic sandstones	34 ± 2	28.43 ± 5.01	−7.24	−20	7.70
	25		Triassic sandstones	35.7 ± 1.2	30.27 ± 5.04	−7.37	−20	7.70

Note. $A_{uncorrected}$ and $A_{corrected}$ stand for ^{14}C activity before and after correction from atmospheric contamination, respectively.

Temperature (°C)	A_0 (pmc)	A_0 model	α1	Latitude	α2	T ($\times 10^{-2}$ m s^{-2})	Sy (%)	L (km)	T (yr)
29.30	39.64 ± 4.95	Eichinger	0.6	29.73	6.82	2.5	2.5	550	9600
31.80	60 ± 7.50	Pearson	0.6	30.52	5.60				
28.50	39.39 ± 4.92	Eichinger	0.6	30.54	5.57				
27.70	42.58 ± 5.32	Eichinger	0.6	31.52	4.36				
30.80	63.33 ± 7.92	Pearson	0.6	31.55	4.33				
33.12	23.99 ± 3.00	Eichinger	0.6	34	2.34	2.5	2.5	25	20
30.00	38.03 ± 4.75		0.6	33.91	2.40				
29.00	26.70 ± 3.34		0.6	33.99	2.35				
26.70	33.12 ± 4.14	Eichinger	0.6	33.39	2.73	2	2.5	30	80
14.40	18.63 ± 2.33		0.6	33.51	2.65				
25.30	18.54 ± 2.32	Eichinger	0.6	33.77	2.48	2.5	2.5	75	180
22.90	22.64 ± 2.83		0.6	33.59	2.60				
25.70	27.42 ± 3.43		0.6	33.77	2.48				
25.50	22.30 ± 2.79		0.6	33.58	2.60				
NA	20.19 ± 2.52	Eichinger	0.6	31.78	4.08	1.5	1.0	210	930
NA	15.00 ± 1.88		0.6	31.75	4.12				
NA	31.07 ± 3.88		0.6	31.56	4.32				
NA	17.60 ± 2.20	Eichinger	0.6	31.96	3.90	2.0	2.5	90	320
NA	44.08 ± 5.51	Pearson	0.6	28.07	10.33	0.5	7.5	50	1190
NA	70.00 ± 8.75		0.6	28.47	9.34				
NA	72.67 ± 9.08		0.6	28.76	8.69				
NA	65.20 ± 8.15	IAEA	0.6	33.68	2.54	1.5	7.5	20	63
23.10	65.61 ± 8.20	IAEA	0.6	32.4	3.50	1.0	7.5	10	16
24.50	32.87 ± 4.11	Eichinger	0.6	33.04	2.98	1.0	2.5	40	127
25.60	33.47 ± 4.18		0.6	33.27	2.81				

promotes atmospheric CO_2 uptake. In order to correct the likely bias associated with this atmospheric contamination, we used here a simplified approach, by considering available comparisons between presumably contaminated and non-contaminated (i.e., small sample volume and Accelerator Mass Spectrometry "AMS" measurement) radiocarbon activity values measured for the same water samples (Aggarwal et al., 2014; Nakata et al., 2016; Yokochi et al., 2018). For this purpose, we adopted the approach proposed by Aggarwal et al. (2014) of a mixing between atmospheric and groundwater sample carbon which is written:

$$A_{\text{cont}} = (1 - f)A_{\text{non-cont}} + fA_{\text{Atm}}, \quad (1)$$

with A_{cont}, $A_{\text{non-cont}}$, A_{Atm}, and f the contaminated, non-contaminated, atmospheric ^{14}C activities, and the fraction of atmospheric carbon introduced in the sample. From the regression line shown in Figure 2, we obtained an average fraction of air contamination of about 8%. Figure 2 also shows that the discrepancy decreases as the activity increases and that the uncertainty represents ca. 100% of the ^{14}C value at low values. Therefore, radiocarbon activity values below 8 pmc obtained with the classical method are largely questionable. On average, the uncertainty on the radiocarbon activity values corrected from atmospheric contamination calculated here was about 5 pmc.

2.3.3. Determination of the A_0 (^{14}C)

A large number of previous studies have been devoted to the discussion of the different processes that may affect the ^{14}C activity of inorganic carbon dissolved in groundwater during its transfer through the vadose zone and along its pathway in the aquifer (e.g., Eichinger, 1983; Fontes & Garnier, 1979). We used here the approach proposed by Han and Plummer (2016) to identify the most appropriate model to estimate the initial ^{14}C activity at the water table (A_0). Following the procedure recommended by these authors, A_0, defined as the ^{14}C content of groundwater after all chemical and isotopic processes have taken place and before

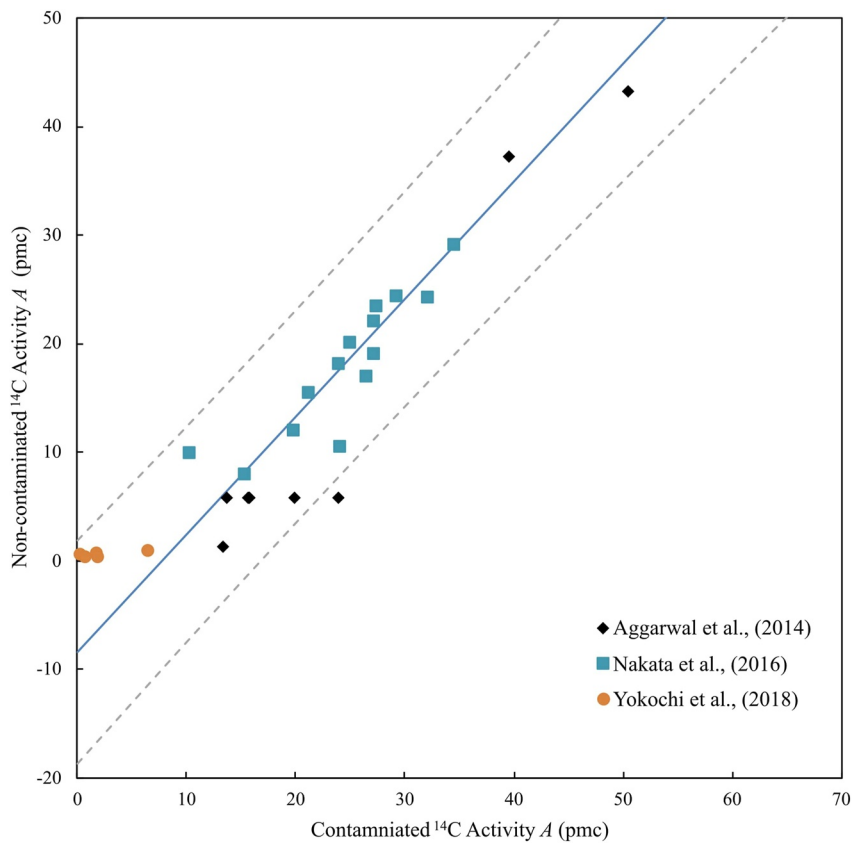

Figure 2. Linear relationship between contaminated and non-contaminated radiocarbon activity data measured for the same water samples (data from Aggarwal et al., 2014; Nakata et al., 2016; Yokochi et al., 2018). Dashed lines are 95% confidence intervals of the regression.

any radioactive decay, is assessed (Table 1). For each radiocarbon sample, we precisely calculate the ^{13}C fractionation factor of carbonate mineral with respect to HCO_3^- ($\varepsilon_{g/b}$), ^{13}C fractionation factor of dissolved CO_2 with respect to gaseous CO_2 ($\varepsilon_{a/g}$), and ^{13}C fractionation factor of carbonate mineral with respect to HCO_3^- ($\varepsilon_{s/b}$). This allowed the construction of the $\delta^{13}C$-^{14}C diagrams following the protocol in Appendix C of Han and Plummer (2016) for each sample, then depicting the ^{14}C $\delta^{13}C$ couplets to identify the appropriate estimation model for A_0. It should be noted that in our A_0 calculations (here, using Eichinger, Pearson, and IAEA models), as Han and Plummer (2016), some approximations were considered, that is, the ^{14}C of soil gas $^{14}C_g = 100$ pmc, ^{14}C of solid carbonate minerals $^{14}C_s = 0$ pmc, and HCO_3^- concentration (C_b) is dominant over CO2 (aq) (C_a) in the total concentration of dissolved inorganic carbon ($C_T = C_a + C_b$), which gives $C_a/C_T \approx 0$ and $C_b/C_T \approx 1$. The most widely selected A_0 model here is the Eichinger's model. However, when the value of A_0 calculated with this model equals the measured activity within the error bars of A and A_0, it was not possible to unequivocally identify which of the Eichinger and IAEA models applies to the sample. Therefore, the approach of Han and Plummer (2016) could not be applied to samples 1, 24, and 25. This is further discussed in terms of alternative empirical model for A_0 estimation in Section 5.

Values of −25‰ and −15‰ for $\delta^{13}C_g$ (Carbon isotopic signature of soil gas CO_2) are ascribed classically to C3 and C4 photosynthetic pathways, respectively. For desert environments dominated by C4 plants, Rightmire and Hanshaw (1973) reported model values for $\delta^{13}C_g$ of −12 ± 5‰ and measured values of −16.7 and −18.2 ± 0.5‰ for two soils. More recently Conaway et al. (2018) provided vadose zone measurements for $\delta^{13}C_g$ of −14.9 ± 3‰. Considering all these estimates, we retained a value of −15 ± 1.5‰ in desert environments. However, considering only present-day vegetation to estimate $\delta^{13}C_g$ could be incorrect due to vegetation changes within the 40 Kyr time period corresponding to the ^{14}C data. Samples 1–5 and 19–21 (Figure 1 and Table 1) are located in areas that have experienced almost exclusively hyper-arid desert climates (Blanchet et al., 2021; Skonieczny et al., 2015; Tjallingii et al., 2008) in the last 40 Kyr, with the exception of the ∼5 Kyr long AHP when herbaceous plains developed with presumably a mixture of C3 and C4 plants (Hély et al., 2014; Lécuyer et al., 2016). Therefore, in these areas of the NWSAS, we assumed a $\delta^{13}C_g$ of −15‰. The remaining samples are located on the north-western and northern borders of the Sahara at the piedmonts of the Atlas, the Northern Chain of Chotts, the Dahar, or the Jebel Nafusa which continuously received higher rainfall amounts during the last 40 Kyr (>100–300 mm yr^{-1}) leading to a mixture of C3 and C4 plants. For these areas, we used the average value of −20 ± 2.5‰ between C3 (−25‰) and C4 (−15‰) plants. Uncertainty on the $\delta^{13}Cg$ was propagated to the initial carbon activity A_0 calculations.

3. Methodology

3.1. Recharge Scenario for the Past 40 Kyr

The general picture of synchronous hydrological changes over North Africa discussed in Section 2.2 allow to reconstruct a schematic recharge scenario based on precipitation reconstructions for the last 40 Kyr (Figure 3) by assuming a linear relationship between annual rainfall and recharge in arid to semi-arid climates (Petersen, 2014; Scanlon et al., 2006). In this square wave scenario, three time periods are considered: (a) Late Pleistocene (−40 to −10 ka, Period I), (b) late Pleistocene to mid Holocene (−10 to −5 ka, Period II), and (c) late Holocene (−5 ka to present day, Period III). The recharge over these periods is defined by $\alpha_i R$, where R is the recent recharge (Period III). For the well-documented Period II, precipitation and recharge reconstructions (Blanchet et al., 2021; Claussen et al., 2013; Hopcroft et al., 2017; Petersen, 2014; Tierney et al., 2017) suggest an average value of 5 ± 2.3 for α_2. However, according to rainfall reconstructions for the AHP provided by Larrasoaña et al. (2013), the AAR increase was proportionally higher in the south of the Saharan belt than in the north, pointing to a latitudinal variation of α_2. Based on that study, we infer a relation between α_2 and latitude λ as: $\alpha_2 = 1.15 \times 10^4 e^{(-0.5*\lambda)}$ between $\lambda = 25°$ and 35°N. Although fewer estimates are available for period I, a value for α_1 of 0.4 can be obtained from Tierney et al. (2017) for the period

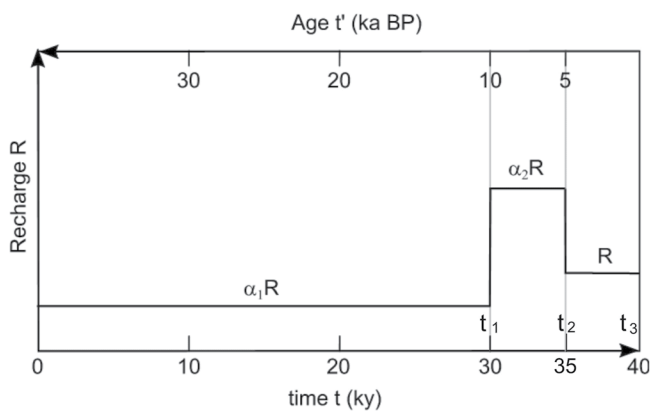

Figure 3. Recharge scenario based on climatic reconstruction for the last 40 Kyr with the time axis used in the models development.

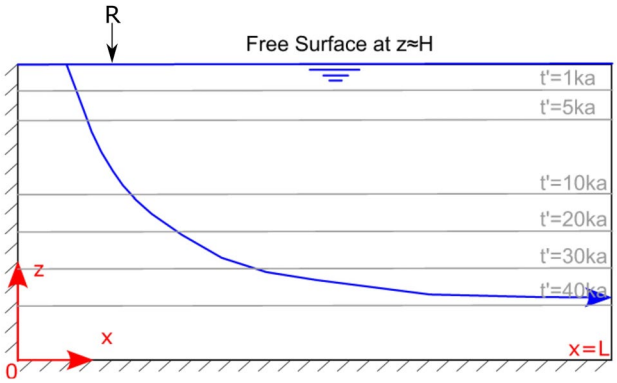

Figure 4. Schematic view of a 2D unconfined aquifer system with the coordinate system used. The *x* axis along the substratum of the aquifer considered is almost horizontal, the *z* axis is vertical upwards, and an almost constant saturated thickness *H* is considered assuming a weak regional gradient of the free surface.

−10 to −25 ka. Climate modeling studies suggest α_1 values between 0.4 and 1 (Alder & Hostetler, 2015; Kageyama et al., 2013) for the LGM (Last Glacial Maximum, −21 ka). Moreover, an exponential relationship can be fitted between AAR/AAR_0 and the aridity index defined by Grant et al. (2017), where AAR_0 is the present-day AAR, using the AAR values for the AHP and the Eemian humid period (−122 to −128 ka) provided by Pausata et al. (2020). We obtain $\alpha_1 = 0.6$ for the period −40 to −10 ka. Based on these different estimates, a value for α_1 of 0.6 ± 0.3 can be considered for the Saharan area. The real influence of the recharge during the glacial period on the ^{14}C vertical profile in an unconfined aquifer is discussed in Section 4.1.

3.2. Models Development

Recharge estimates were obtained from radiocarbon data along selected streamlines within a clearly identified geological formation by means of a particle tracking approach based on velocity field assessment. We considered here a 2D cross-section *(x,z)* for a simple unconfined aquifer with constant hydraulic parameters (hydraulic conductivity and porosity), being recharged by precipitation over its whole outcrop as shown in Figure 4. In this situation, the two-component velocity field leads to a downstream water particle movement from the water table receiving a recharge *R* to some location *(x(t), z(t))*. Strictly speaking, the 2D free-surface aquifer problem requires solving the continuity equation:

$$\mathrm{div}\left(\vec{q}\right) = \frac{\partial q_x}{\partial x} + \frac{\partial q_z}{\partial z} = 0 \tag{2}$$

with a boundary condition at the free-surface which is written in the bi-dimensional case according to Bear (1979):

$$K_x \frac{\partial h}{\partial x}\frac{\partial \zeta}{\partial x} - K_z \frac{\partial h}{\partial z} + R = S_y \frac{\partial \zeta}{\partial t} \tag{3}$$

Equation 3 was obtained using a mass balance equation at the moving phreatic surface, where q_x and q_z and K_x and K_z are the specific discharge (m s^{-1}) and the hydraulic conductivities along the *x* and *z* directions, *R* is the recharge (m s^{-1}), *ζ(x,t)* is the free phreatic surface elevation (m), *h(x,z,t)* is the hydraulic head (m), and S_y is the dimensionless specific yield. From a practical standpoint, Equation 3 can be solved numerically for *ζ(x,t)* using an explicit scheme. Then Equation 2 combined with Darcy's Law can be solved for *h(x,z,t)* within the domain below the water table (Bear et al., 2010).

In this study, we adopted alternative approaches to this purely numerical solution based on an extension of the simple analytical model proposed by Vogel (1967) which is briefly outlined below. Using a steady state mass balance analysis and under the simplifying assumption of temporally and spatially constant recharge and saturated thickness, Vogel (1967) derived particle tracking parametric expressions:

$$t' = \frac{\omega H}{R}\ln\left(\frac{x}{x_0}\right) \tag{4}$$

and:

$$t' = \frac{\omega H}{R}\ln\left(\frac{H}{z}\right) \tag{5}$$

where *t'* is the hydrodynamic age (yr) of a fluid particle entering the saturated zone at a location x_0 (m) and $t' = 0$, *H* (m) is the aquifer's saturated thickness, *z* (m) is the upward vertical axis with the origin at the substratum of the aquifer and *ω* is claimed by the author to be the total porosity and not the drainage porosity. It can be verified that the integration of Equation 5 over the vertical saturated thickness:

$$\tau_R = \frac{1}{H}\int_{z=0}^{z=H} \frac{\omega H}{R} \ln\left(\frac{H}{z}\right) dz \tag{6}$$

which leads to the expression of the groundwater residence time for an unconfined aquifer:

$$\tau_R = \frac{\omega H}{R} = \frac{\omega A_s H}{R A_s} \tag{7}$$

where A_s (m^2) is the surface area of the aquifer, $\omega A_s H$ represents the total groundwater volume, and RA_s is the inflow. Moreover, according to Equation 5, the age and thus the ^{14}C distribution only depends on z and not on the location x under the conditions used for the calculation. Noting that the infinitesimal displacement which must be integrated to obtain Equations 4 and 5 is related to the velocities as follows:

$$dx = v_x dt; dz = v_z dt \tag{8}$$

the underlying pore velocity components v_x and v_z ($m\ s^{-1}$) can be written as:

$$v_x = \frac{R}{\omega H} x; v_z = -\frac{R}{\omega H} z \tag{9}$$

The expression for v_x in Equation 9 can be in fact directly derived from the mass balance considered by Vogel (1967). However, this groundwater mass balance implies using the kinematic porosity ω_c and not the total porosity ω. Indeed, noting that the x component of the velocity simply corresponds to the cumulated volume which entered the unconfined system at a distance x (m) from the upstream zero flux boundary (see Figure 4), the water balance equation per meter perpendicular to the flow direction is written:

$$R \times x = q_x \times H = v_x \times \omega_c \times H \tag{10}$$

It is thus assumed that the total porosity ω almost equals the kinematic porosity ω_c which is an approximation (Marsily, 1986) valid for porous media with low specific surface (e.g., sand) and/or low solid surface reactivity. The linear relationship between v_z and z is often reported as a postulate in Vogel's calculation (e.g., McMahon et al., 2011) but it is in fact a requirement of the continuity equation (Equation 2). Indeed, it can be seen that Vogel's expressions can be written as $q_x = -K_x\left(\partial h/\partial x\right) = \left(R/H\right)x$ and $q_z = -K_z\left(\partial h/\partial z\right) = -\left(R/H\right)z$, satisfying Equations 2 and 3 at steady state, and for a phreatic surface at $z = \zeta = H$ noting that $-K_x\left(\partial h/\partial z\right)|_{z=\zeta=H} = -\left(R/H\right)\zeta = -R$ in Equation 3. The latter condition corresponds to the assumption of an almost constant saturated thickness made by Vogel (1967) as depicted in Figure 4. Vogel's solution is thus restricted to steady-state conditions, which is a serious limitation considering the Quaternary climate, and thus recharge rate, variations. Therefore, radiocarbon interpretations using this solution lead at best to average recharge values over the investigated period (Wood et al., 2015) without the averaging formalism enabling the reconstruction of temporal changes in recharge to be known.

Extending Voge's model requires identifying transient analytical expressions accounting for temporal variations in recharge. Two sets of expression were developed here: a TS model, and a PSS model.

TS model: The first set of approximate expressions for the velocity field was obtained by means of a numerical solution of Equations 2 and 3 for a base case as described in Appendix A. For this solution, we considered an instantaneous increase in the recharge from 0 to R at $t = 0$ together with $h(x, t = 0) = H$ as the initial condition, and the following boundary conditions: $h = H$ at $x = L$, $q_z = 0$ at $z = 0$ and $q_x = 0$ at $x = 0$. Assuming a constant saturated thickness (weakly variable) similarly to Vogel (1967) yields:

$$q_x\left(x,t\right) = \frac{R}{H}\left[\exp\left(-\frac{2t}{\tau}\right)\frac{x^2}{2L} + \left(1 - \exp\left(-\frac{2t}{\tau}\right)\right)x\right] \tag{11}$$

and:

$$q_z\left(x,z,t\right) = -\frac{R}{H}\left[\exp\left(-\frac{2t}{\tau}\right)\frac{x}{L} + \left(1 - \exp\left(-\frac{2t}{\tau}\right)\right)\right]z \tag{12}$$

where τ is the characteristic time of the aquifer: $\tau = \left(L^2/D_h\right)$, with $D_h = T/S_T$ the hydraulic diffusivity ($m^2\ s^{-1}$), T the transmissivity of the aquifer ($m^2\ s^{-1}$), S_T the dimensionless storativity which is the specific yield S_y, or the storage coefficient S for an unconfined or a confined aquifer, respectively.

The characteristic time is associated with pressure transfer and is used to describe the time needed to reach a new steady state after a major change in surface boundary conditions such as the recharge rate (see, e.g., Rousseau-Gueutin et al., 2013). The solution proposed in Appendix A points to a steady-state almost reached after 2τ which is slightly faster than the 3τ reported by Rousseau-Gueutin et al. (2013). Moreover, a small average difference of about 5% with the steady state in terms of velocity field is obtained after 1τ. This more rapid response may be attributed to pressure diffusion in both x and z directions and not only in the x direction classically accounted for by considering Dupuit's (1863) assumption for fluid flow. Using Equations 11 and 12 in a particle tracking approach leads to a relatively limited error in the location of a fluid particle, in comparison to the more complex numerical solution, of a few hundreds of meters in x and a few tens of centimeters in z (see Appendix A). Therefore, these approximate analytical expressions allow simple particle tracking calculations without the need for numerical solution and are therefore particularly convenient. For large t values ($t \to \infty$), it is verified that Equations 11 and 12 tend to the steady state expressions by Vogel (1967). The complete expressions for q_x and q_z applying to the recharge scenario proposed here (see Figure 3) can be obtained by convolution. Naming the right hand side of Equations 11 and 12 $f(x,t,R)$ and $g(x,z,t,R)$, respectively, the convolution can be written:

$$\begin{cases} q_x = f\left(x, t, \alpha_1 R\right) & \text{if } 0 \le t < t_1 \\ q_x = f\left(x, t, \alpha_1 R\right) + f\left(x, t - t_1, \left(\alpha_2 - \alpha_1\right) R\right) & \text{if } t_1 \le t < t_2 \\ q_x = f\left(x, t, \alpha_1 R\right) + f\left(x, t - t_1, \left(\alpha_2 - \alpha_1\right) R\right) + f\left(x, t - t_2, \left(1 - \alpha_2\right) R\right) & \text{if } t_2 \le t < t_3 \end{cases} \tag{13}$$

and:

$$\begin{cases} q_z = g\left(x, z, t, \alpha_1 R\right) & \text{if } 0 \le t < t_1 \\ q_z = g\left(x, z, t, \alpha_1 R\right) + g\left(x, z, t - t_1, \left(\alpha_2 - \alpha_1\right) R\right) & \text{if } t_1 \le t < t_2 \\ q_z = g\left(x, z, t, \alpha_1 R\right) + g\left(x, z, t - t_1, \left(\alpha_2 - \alpha_1\right) R\right) + g\left(x, z, t - t_2, \left(1 - \alpha_2\right) R\right) & \text{if } t_2 \le t < t_3 \end{cases} \tag{14}$$

Combining Equations 11–14 in a particle tracking approach yields the hydrodynamic age distribution which can be combined with the radiocarbon exponential decay equation:

$$t' = t_3 - t = \frac{1}{\lambda} ln\left(\frac{A_0}{A}\right), \tag{15}$$

where A_0 (pmc), the initial ^{14}C activity of the TDIC assessed following Han and Plummer method (see above), A (pmc) is ^{14}C activity, and $\lambda = 1.21 \times 10^{-4}\ yr^{-1}$ is the radioactive decay constant for ^{14}C.

This allows us to calculate the (x,z) activity distribution and vertical profiles that constitute the TS model. From a practical standpoint, the path of a fluid particle entering the aquifer at the free-surface and at time t ($x = x_0$ and $z = H$) can be calculated using this solution to establish its present-day location in a forward approach. Backwards particle tracking from a given present-day profile at a location x can be performed as well. The latter approach can thus be used to fit the radiocarbon data.

3.2.1. Pseudo Steady State Model (PSS)

These hydrodynamic age model calculations can be greatly simplified if the characteristic time τ which governs the reactivity of aquifers is low. This is the basis of the second interpretation model (PSS). In such a case, the aquifer is very reactive, leading to a succession of steady states separated by very short intermediate TS. Indeed, if $\tau << 5$ Kyr, the velocity field adjusts almost instantaneously to the square wave time function for the temporally varying recharge considered here (see Appendix A). The TS can then be largely neglected, yielding a very simple extension of Vogel's solution in a pseudo-steady state approach (making τ

tend to 0 in Equations 12 and 14). In this case q_z only depends on z and t, and the relation between A and z can be established (see Appendix A) and written as follows:

$$\begin{cases} \frac{A}{A_0} = \left(\frac{z}{H}\right)^{\beta_1} & if\ z_2 < z \le H \\ \frac{A}{A_0} = \beta_2\left(\frac{z}{H}\right)^{\beta_3} & if\ z_1 < z \le z_2 \\ \frac{A}{A_0} = \beta_4\left(\frac{z}{H}\right)^{\beta_5} & if\ z_0 < z \le z_1 \\ \frac{A}{A_0} = 0 & if\ z \le z_0 \end{cases} \tag{16}$$

where

$$\beta_1 = \frac{H\omega\lambda}{R}; \beta_3 = \frac{H\omega\lambda}{\alpha_2 R}; \beta_5 = \frac{H\omega\lambda}{\alpha_1 R} \tag{17}$$

$$\beta_2 = \exp\left(-\frac{\lambda}{\alpha_2}\left(t_3 - t_2\right)\left(\alpha_2 - 1\right)\right) \tag{18}$$

$$\beta_4 = \exp\left(\lambda\left(t_1 - t_3\right) + \frac{\lambda\alpha_2}{\alpha_1}\left(t_2 - t_1\right) + \frac{\lambda}{\alpha_1}\left(t_3 - t_2\right)\right) \tag{19}$$

$$z_0 = H\exp\left(-\frac{\alpha_1 R t_1}{\omega H} - \frac{\alpha_2 R}{\omega H}\left(t_2 - t_1\right) - \frac{R}{\omega H}\left(t_3 - t_2\right)\right) \tag{20}$$

$$z_1 = H\exp\left(-\frac{\alpha_2 R}{\omega H}\left(t_2 - t_1\right) - \frac{R}{\omega H}\left(t_3 - t_2\right)\right) \tag{21}$$

$$z_2 = H\exp\left(-\frac{R}{\omega H}\left(t_3 - t_2\right)\right) \tag{22}$$

The z coordinates z_0, z_1, z_2 correspond to the vertical location of the particles which were at the water table 40, 10, and 5 Kyr ago. Note that if $\alpha_1 = \alpha_2 = 1$, Vogel's solution should be recovered. Introducing Equation 15 into Equation 5 gives the activity vertical profile associated with Vogel's model which is written:

$$\frac{A}{A_0} = \left(\frac{z}{H}\right)^{\beta} \tag{23}$$

where $\beta = \left(H\omega\lambda/R_A\right)$, with R_A the constant long-term average recharge (m yr^{-1}). Setting $\alpha_1 = \alpha_2 = 1$ in Equations 16–22, that is, $R = R_A$, leads to $\beta_1 = \beta_3 = \beta_5 = \beta$ and $\beta_2 = \beta_4 = 1$. Therefore, Vogel's solution is effectively recovered except for the bottom of the saturated column ($z \le z_0$) where the discrepancy with Vogel's solution is only due to the assumption $A = 0$ for $t' > 40$ ka BP ($t = 0$ at $t' = 40$ ka BP for model development, Figure 3). However, as this bias related to bottom old groundwater represents less than 1% of the vertically averaged activity value considered here (see Section 4.1), Vogel's solution is approximately retrieved.

For both models (PSS and TS), assuming a uniform contribution of the vertically stratified streamlines during sampling, the measured activity of samples collected using large pumping rate equipment and thus resulting from a vertical mixing, can be compared with the theoretical average value which is analytically written:

$$\overline{A} = \frac{1}{H}\int_0^H A\left(z\right)dz \tag{24}$$

where $A(z)$ is given by Equations 13–15 or Equations 16–22.

For instance, introducing the PSS solution (Equations 16–22 into Equation 24) gives:

$$\overline{A} = \frac{A_0}{H}\left[\frac{\left(H^{\beta_1+1} - Z_2{}^{\beta_1+1}\right)}{\left(\beta_1+1\right) * H^{\beta_1}} + \frac{\beta_2\left(Z_2{}^{\beta_3+1} - Z_1{}^{\beta_3+1}\right)}{\left(\beta_3+1\right) * H^{\beta_3}} + \frac{\beta_4\left(Z_1{}^{\beta_5+1} - Z_0{}^{\beta_5+1}\right)}{\left(\beta_5+1\right) * H^{\beta_5}}\right] \tag{25}$$

while using Vogel's steady-state solution (Equation 23) simply gives:

$$\overline{A} = \frac{A_0}{\left(\beta+1\right)} \tag{26}$$

4. Results

4.1. Comparative Analysis of Models for Radiocarbon Interpretation

Here, it was first verified that using Vogel's steady-state solution results in a long-term recharge whose averaging formula must be ascertained when possible. For this purpose, Equations 16–22 were solved in order to compare the results obtained by the analytical model of Vogel (1967) with a constant recharge, and our PSS model with a square wave recharge scenario. Given that the samples are in most cases collected with high-rate pumps and thus represent a mixing, average ^{14}C activity calculated along the profiles was considered. The PSS base case used here corresponds to $L = 100$ km, $H = 100$ m, $\omega = 0.1$, $R = 1$ mm yr^{-1}, $A_0 = 50$ pmc, $\alpha_1 = 0.6$, and $\alpha_2 = 5$ leading to a vertically average activity value of 28.1 pmc (Figure 4). This average value can also be obtained using Vogel's model given that the long-term average recharge corresponding to our base case recharge scenario is known. From a theoretical standpoint, the average value can be found by equating Equations 25 and 26, therefore establishing the required averaging formula to obtain R_A. Applying this average value yields $R_A = 1.55$ mm yr^{-1} which was introduced in Vogel's expression (Equation 23). The calculated ^{14}C activity vertical profiles with the same average value at 28.1 pmc for the two models are depicted in Figure 5. Figure 5 shows that the discrepancy between the two profiles is higher at intermediate depths, between $z_1 = 5$ m (red line) to $z_2 = 60$ m (blue line), which corresponds to the higher recharge during Period II. In addition, given the low contribution of the most ancient recharge before Period I, only a low ^{14}C activity appears at the bottom of the aquifer below the green line $z_0 < 1$ m, representing less than 1% of the vertically averaged ^{14}C activity $\overline{A}$. With respect to the interpretation of radiocarbon samples, our calculations confirm that a long-term average recharge (here, $R_A = 1.55$ mm yr^{-1}) and not the present-day recharge (here, $R = 1$ mm yr^{-1}) is obtained when using Vogel's standard solution. This is further discussed for the case of North African aquifers in Section 5. The refined analysis of a constant average value inferred from Vogel's model in terms of time-varying recharge and especially of present-day value is only possible if the theoretical expression for the temporal variation is known. While relatively straightforward in the pseudo-steady-state case as illustrated here, this becomes much more difficult in the most general case of Ts.

Using the same base case aquifer geometry (100 m × 100 km), we analyzed the sensitivity of our TS model to the characteristic time τ and the influence of the transient behavior in terms of radiocarbon interpretation. Figure 6 shows the calculated 2D age contour plots produced with the TS model for different values of characteristic time (τ) of the aquifer. This analysis illustrates the transient effect on the age distribution, thus on the ^{14}C activity profiles as a function of the distance x (upstream-downstream effect). Figure 6 shows that, using the same climatic scenario as in PSS calculations ($R = 1$ mm yr^{-1}, $\alpha_1 = 0.6$, and $\alpha_2 = 5$), the transient behavior (large τ values) produces an upstream sloping of the age contour lines corresponding to younger groundwater upstream at a given depth. Therefore, the calculated vertical means of ^{14}C activity decrease downstream (Figure 6d). This can be explained by the fact that the most recent velocity field (notably qz) remains influenced by the AHP high water velocity conditions, especially upstream due to inertial transient effects (see Equation 12). This theoretical result is well illustrated by the ^{14}C activity data for the "Grand Erg Oriental" (Table 1), where a downstream decrease of about 11 pmc is observed along the 220 km streamline

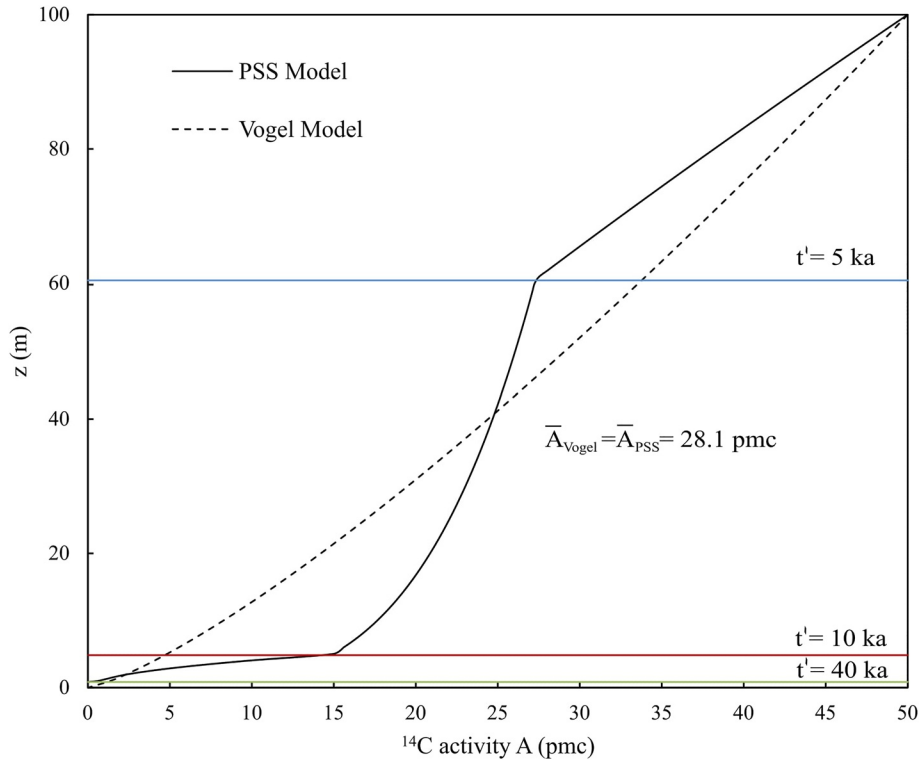

Figure 5. ^{14}C activity profiles calculated using the PSS model and Vogel's model. $\overline{A}_{Vogel}$ and $\overline{A}_{PSS}$ are the vertically averaged activities for the Vogel and PSS model, respectively. The profiles were estimated for a base case using L = 100 km, H = 100 m, R = 1 mm yr^{-1}, R_A = 1.2 mm yr^{-1}, α_1 = 0.6, α_2 = 5, ω = 0.1, and A_0 = 50 pmc.

(characteristic time τ at 9,600 years). The transient effect is smaller for τ = 1,000 years and almost negligible at τ = 100 years which produce the same hydrodynamic age distribution as the PSS simulation.

4.2. Recharge in the Saharan Area

Following the protocol explained above, we used Equations 13–15 and Equation 25 to determine the present-day recharge value for eight aquifer systems selected according to our list of criteria. Among the 25 data points that we had selected, we distinguished eight outcropping areas: four areas for the CT aquifer, three outcrops for the CI aquifer, and the area corresponding to the free-surface outcrop of the mostly confined Triassic aquifer in the Djeffara plain (Figure 1). Our results are reported in Table 2, along with the characteristic time (τ) of each system, and thus the analytical model (PSS or TS) which was used.

A constant saturated thickness H_{model} was considered for each formation along the streamline of interest (see Figures 1b and 1c and Table 1). We considered average porosity values of ω = 0.18 ± 0.01 for the CT (between 15% and 20% according to Pallas, 1972, as cited in Swezey, 1999), $\omega = 0.22X \pm 0.015$ for the CI in the NWSAS area (average value for CI according to ERESS, 1972), and ω = 0.065 ± 0.008 for the Djeffara aquifer (between 5% and 8% according to OSS, 2006). The quoted uncertainties were estimated by considering the porosity ranges as 95% confidence intervals of a normal distribution. The radiocarbon data were then interpreted using either the PSS or TS expressions with a specific parameter set (α_1, α_2, H_{model}, and A_0) listed in Table 1. The recharge rates calculated at each sampling site were then averaged to obtain the regional values at the eight outcropping areas upstream of the streamlines depicted in Figure 7. Recharge values between 0.2 ± 1.7 and 4.5 ± 3.2 mm yr^{-1} were obtained, with the highest values in the northern outcrops of the Atlas for the CI and the Trias for the Djeffara plain. By contrast, low values were obtained for the Northern Chain of the Chotts (1.5 ± 1.2 mm yr^{-1}) in spite of a relatively high AAR of 150 mm yr^{-1}. The lowest values were found in the CI of the Tinhrert area, in the southern part of the NWSAS where AAR of only a few mm per year were recorded.

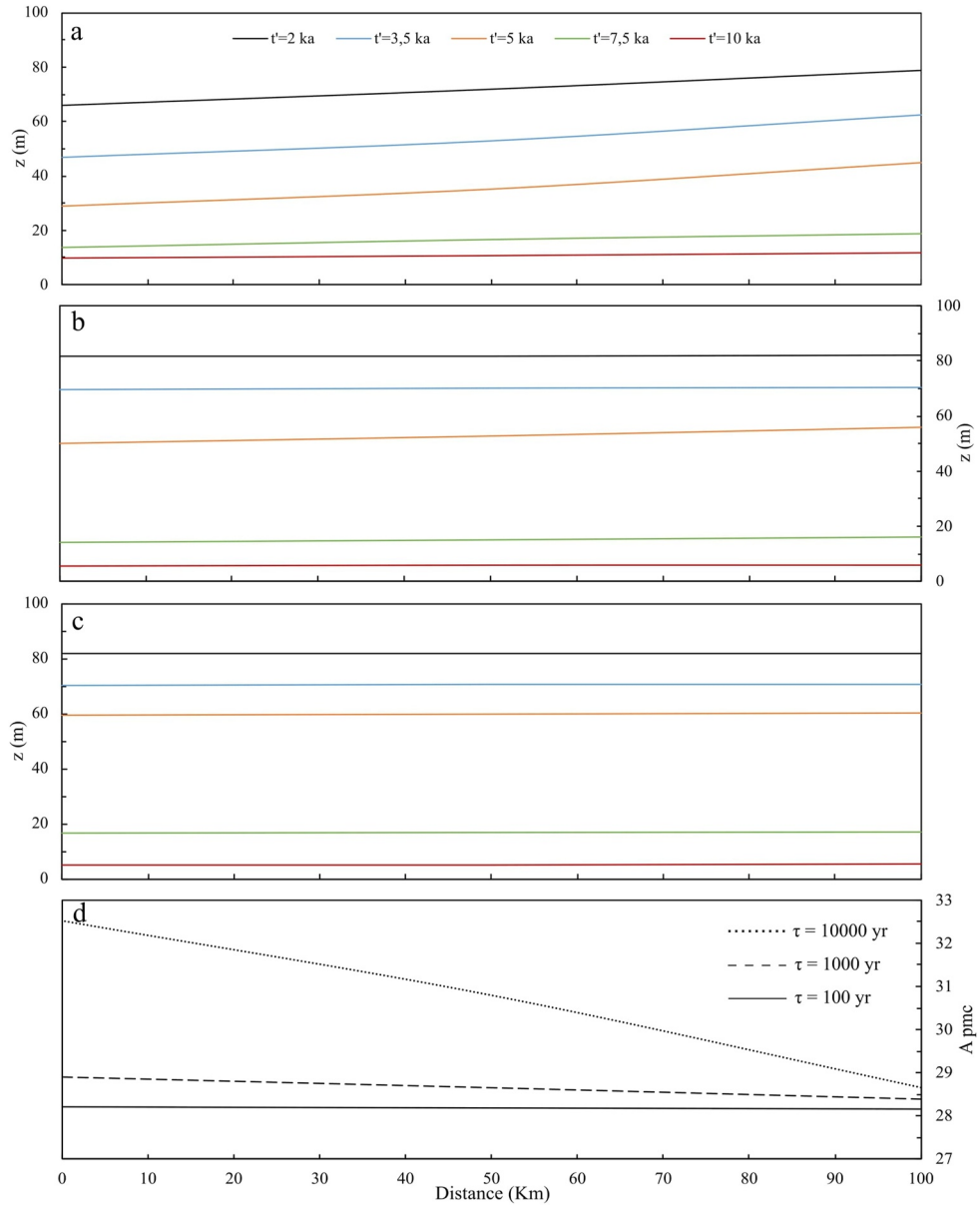

Figure 6. Calculated hydrodynamic age contour lines: 2, 3.5, 5, 7.5, and 10 ka; using the TS model for three τ values, that is, (a) τ = 10,000 years, (b) τ = 1,000 years, (c) τ = 100 years. (d) Calculated vertical mean of ^{14}C activity as a function of the distance x for each τ value. Solutions were calculated for a base case using L = 100 km, H = 100 m, R = 1 mm yr^{-1}, α_1 = 0.6, α_2 = 5, ω = 0.1, and A_0 = 50 pmc.

In arid environments, a clear relationship is expected between recharge and precipitation, due to the scarcity of vegetation (Keese et al., 2005; Scanlon et al., 2006). Our results illustrate the linear relationship between the present-day AAR and mean annual recharge for the different recharge zones considered here (Figure 7). The regression line suggests that under a very low AAR, a diffuse discharge occurs as measured in the southwestern Sahara by Fontes et al. (1986).

The linear relationship between AAR and recharge can then be used to assess the regional distribution of the present-day recharge of Saharan aquifers as shown in Figure 8. This estimation is based on the available AAR data from the CRU (http://wps-web1.ceda.ac.uk). Excluding the confined areas of the NWSAS (~350,000 km^2; Baba Sy, 2005), the domain-averaged recharge estimates are 1.6 ± 2.3 and 3.5 ± 2.3 mm yr^{-1}, for NWSAS and the Djeffara, respectively. Note that the uncertainties considered here

Table 2
Recharge Rates at Outcrop Areas of Saharan Aquifers: CT, CI, and Djeffara Based on ^{14}C Data Interpretation

Recharge zone	Sample	H model (m)	Model	^{14}C (pmc)	R (mm yr^{-1})	R zone (mm yr^{-1})	P (mm yr^{-1})
Grand Erg Oriental CT	1	120	TS	37.65 ± 5.19	NA	1.30 ± 0.27	40
	2			33.74 ± 5.11	1.53		
	3			21.92 ± 4.93	1.50		
	4			18.34 ± 4.91	1.15		
	5			25.61 ± 4.97	1.03		
Northern Chain of Chotts CT	6	200	PSS	4.03 ± 4.94	0.71	1.53 ± 1.17	150
	7			11.40 ± 4.90	1.48		
	8			10.86 ± 4.90	2.40		
Dahar CT	9	300	PSS	24.31 ± 4.96	16.43	4.26 ± 0.75	134
	10			10.97 ± 4.90	7.61		
	11	100	PSS	3.70 ± 4.95	0.43		
	12			4.90 ± 4.93	0.46		
	13			4.79 ± 4.93	0.36		
	14			3.27 ± 4.95	0.29		
Nafusa CT	15	300	PSS	1.75 ± 4.97	0.38	3.63 ± 0.86	136
	16			5.44 ± 4.93	2.28		
	17			16.50 ± 4.90	4.85		
	18	200	PSS	11.73 ± 4.90	7.01		
Tinhrert CI	19	100	PSS	16.28 ± 4.90	0.44	0.20 ± 1.70	2
	20			10.32 ± 4.90	0.13		
	21			2.29 ± 4.96	0.03		
Atlas CI	22	150	PSS	54.13 ± 5.69	4.50	4.50 ± 3.20	290
Dahar CI	23	150	PSS	42.24 ± 0.21	2.30	2.30 ± 0.67	125
Djeffara	24	200	PSS	28.43 ± 5.01	1.00[a]	3.50 ± 1.54[a]	180
	25			30.27 ± 5.04	6.00[a]		

Note. "NA" stands for "Not Applicable."
[a]Recharge rates that are calculated with A_0 estimated by an empirical approach (see Section 5).

are those associated with the linear regression with a 95% confidence intervals. These recharge values correspond to 1.1 ± 1.5 km^3 yr^{-1} on the 650,000 km^2 of outcropping areas of the CI and CT aquifers of the NWSAS, and 0.17 ± 0.1 km^3 yr^{-1} on the 48,000 km^2 of the Djeffara plain.

5. Discussion

The results described above show that our 2D-analytical expressions (TS and PSS) constitute a practical-use alternative solution to more complex 3D simulations using fluid flow and reactive transport models, which require more information, precise data, and are possibly affected by equifinality issues during calibration (i.e., many combinations of calibration variables can reproduce the observed data).

For highly reactive systems such as the free-surface outcrops of the large-scale confined CI aquifer, the recharge can be simply and accurately obtained using the pseudo-steady state PSS model. This concerns 7 of the 8 outcrop areas considered in our study, representing 20 out of the 25 samples. On the other hand, for less reactive formations such as the CT outcrops at the "Grand Erg Oriental" (Figure 1), the TS model must be used. The benefits of such approaches can be illustrated by comparing the results obtained using the expressions developed in this study, with the recharge values interpreted using Vogel's fully

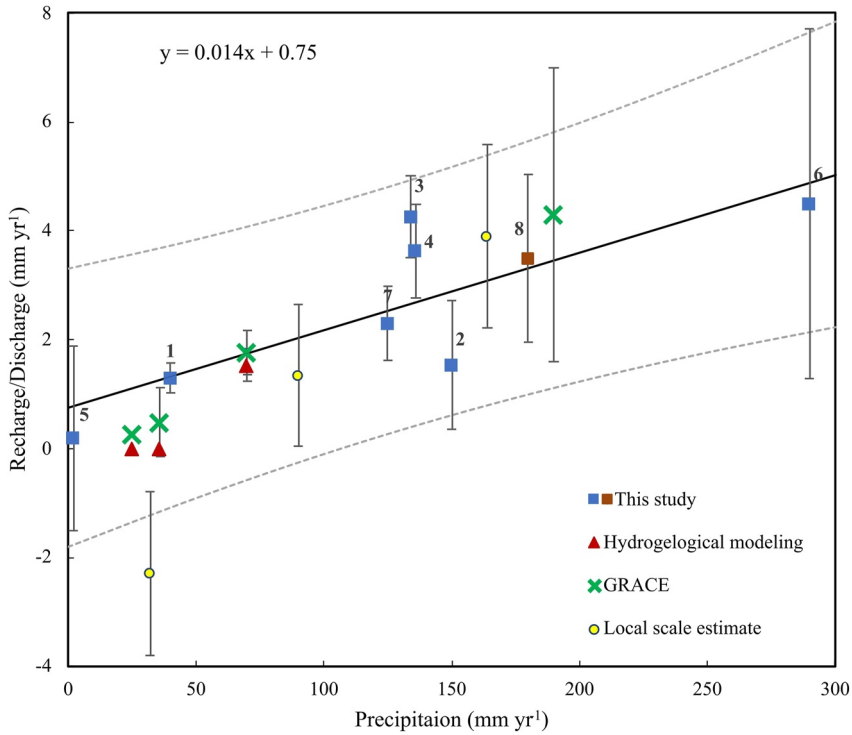

Figure 7. Calculated recharge (or discharge, negative values) as a function of AAR for eight recharge outcrop areas of Saharan Aquifers (see Figure 1 for outcrop area name associated to each number), and values obtained at different scales with different methods from other studies for Saharan belt aquifers (NWSAS, Murzuk, and Nubian Sandstone Aquifer System NSAS): regional scale (106 km^2, GRACE, hydrogeological modeling), local scale (10^1 m^2). The plain line represents the linear regression between precipitation and calculated recharge. This concerns outcrops No. 1–7, Djeffara (outcrop No. 8) recharge rate calculated using an empirical approach for A_0 estimation (see Section 5) was not considered for the linear regression. Dashed lines are 95% confidence intervals of the regression.

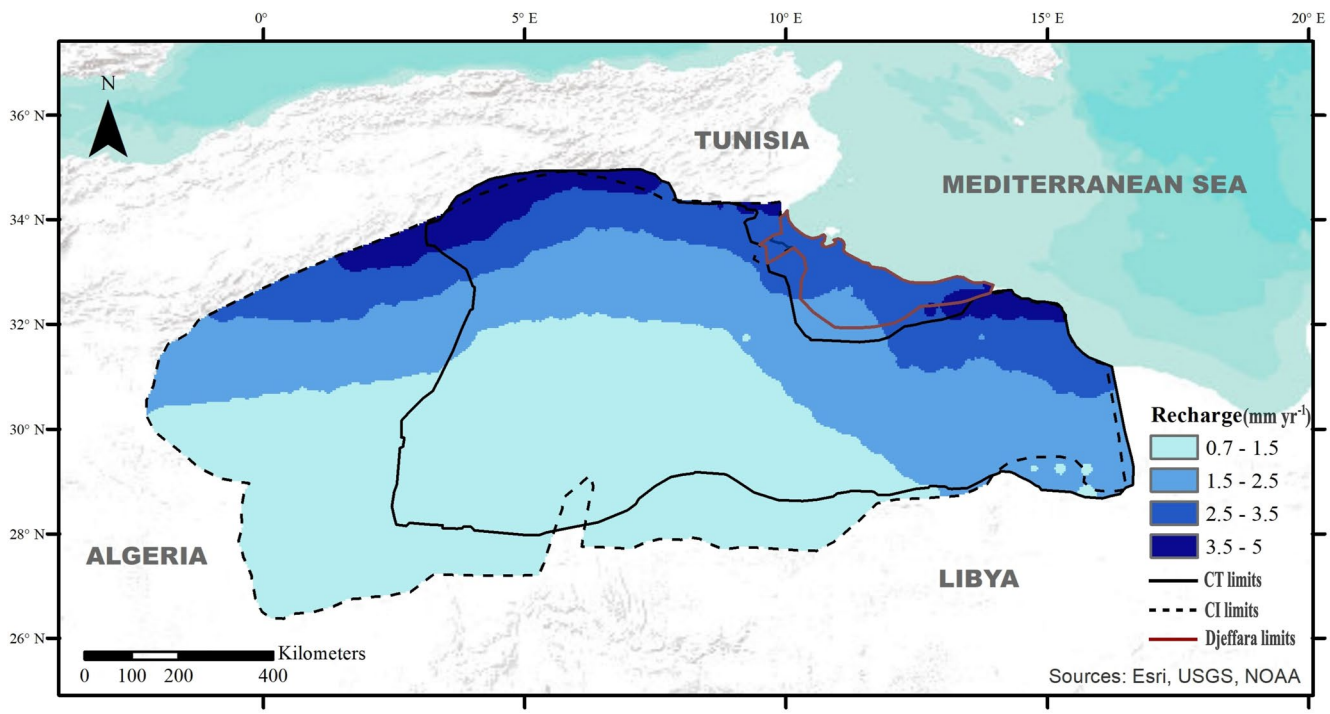

Figure 8. Calculated recharge map for the study area using the linear regression between calculated recharge and precipitation shown in Figure 7 and precipitation estimates provided by the CRU. The confined parts were excluded in the calculations of the overall recharge of the NWSAS.

steady-state standard model and the same data set. The latter approach led to globally higher recharge values. Therefore, considering these values as present-day recharge estimates is an overestimation. For the data set used here for North African aquifers, the overestimation ranges from 4% to 360% with a mean value of 74%. Recharge estimates identified using Vogel's solution are influenced by the AHP, showing that some average value and not the present-day recharge is obtained. Nevertheless, present-day recharge is required for hydrogeological modeling implementations where a pre-industrial steady-state is often postulated but not argued. The high reactivity of the CI was already discussed by Petersen (2014) and Gonçalvès et al. (2020). Here we can examine in the same way the global characteristic time for the CT. Considering a mean streamline length of 300 km, an average transmissivity of 2×10^{-2} m^2 s^{-1}, and an average specific yield of 2% (Baba Sy, 2005), we obtain a characteristic time of about 2,800 years. This justifies the assumption of a nearly steady-state in 1950 made by Baba Sy (2005), given that the last recharge variation occurred ~5 Kyr ago, which was the basis for the reference TS hydrogeological model of the NWSAS.

The approach developed here is nevertheless sensitive to data quality. Uncertainties of assessed recharge on the order of 1 mm yr^{-1} are mostly related to correction of the radiocarbon activity A measurement (see discussion in Section 2.3), but also, to initial activity A_0 calculations. The method by Han and Plummer (2016) to identify A_0 could not be unequivocally applied for three out of the 25 selected data preventing obtaining a radiocarbon-based recharge estimate for the Djeffara plain (see Section 2.3). However, an empirical approach to estimate the initial radiocarbon activity based on the relation between vadose zone radiocarbon data and depths to the water table (Irvine et al., 2021) can be alternatively used. For the Djeffara samples, long-term natural values for the unsaturated zone thickness can be derived using piezometric levels in 2006 and the cumulative drawdown from the steady state (OSS, 2006; Trabelsi et al., 2009), and ground elevation giving 30 and 60 m for samples 24 and 25, respectively. Introducing these values into the expression provided by Irvine et al. (2021) gives A_0 at 63 and 37.9 pmc for samples 24 and 25. Using these values for A_0 in the PSS model leads to the mean recharge at 3.5 mm yr^{-1} indicated in Table 2. This point depicted in Figure 6 shows good consistency with the linear relation between recharge and AAR.

The recharge scenario proposed here is also a rough simplification of climate variability over the investigated area. Furthermore, the simplicity of the proposed models requires the use of selection criteria for radiocarbon data which restricts the amount of data retained for interpretations. Among the 184 samples of radiocarbon data collected from the literature, only 14% enable a simple interpretation. For instance, only 4 data samples were retained out of the 39 reported by Gonfiantini et al. (1974). Most of the wells sampled by Gonfiantini et al. (1974) were located in the southwestern part of the CI, in the region of the Foggaras (Figure 1) which is the main discharge area of this aquifer. In this area, the streamlines coming from the recharge zone from the Atlas domain mix with the local recharge. In this case, more complex models are required to consider mixing issues and to deal with deep 3D multi-layer aquifers.

Our analysis assumes that the sample represents a perfect mixing of the stratified streamlines during sampling by pumping. This relies on Dupuit's hypothesis of the horizontal convergence of stratified streamlines, vertically constant values of both the horizontal hydraulic conductivity K_x and the radial hydraulic head gradient, and therefore the discharge. This simplification justifies focusing on specific geological formations (criteria of data selection). Moreover, it should be noted that an advection-dominated transport is considered, thus neglecting dispersion which could generate a bias as recently discussed by Cartwright et al. (2020). However, this hypothesis can be supported by the estimated dispersivity coefficients as a function of the length scale of the flow, as proposed by Gelhar et al. (1992) for various aquifers, together with the activity gradient values along the streamlines (x direction). A dispersivity of between 250 and 1,000 m for a 10^5 m length scale of our streamlines as given by Gelhar et al. (1992), together with the low values of the activity gradient (dA/dx) suggest that the convective term largely dominates over dispersion.

In the approach proposed here, we maintained the standard Vogel's model assumption of a constant recharge along a streamline which therefore represents an average spatial value. In case of exclusive focused recharge, this assumption could be largely questionable. However, diffuse recharge was clearly identified for different aquifers of the Saharan belt (Edmunds, 2001; Yermani et al., 2009). In addition, focused recharge represents less than 30% of the total recharge in the Djeffara plain according to

OSS (2006) using hydrological water balance calculations and hydrogeological modeling. Therefore, in spite the real fractions of focused and diffuse recharge remain unknown, the constant (average) recharge represents a reasonable and convenient simplifying assumption allowing the development of practical use hydrodynamic age models for radiocarbon interpretation. Recharge mechanisms are rather complex and are controlled by climate, vegetation, geology, and are dependent on, for example, rainfall events and soil moisture (see, e.g., Keese et al., 2005). However, regarding long term average annual recharge, simple power law or polynomial relations with the long-term average annual rainfall were proposed: power law using 1D variably saturated model simulation (Keese et al., 2005) or using recharge data collection and an empirical relation (MacDonald et al., 2021), linear relation using recharge data in arid domain (Scanlon et al., 2006). The simple linear relation described by Scanlon et al. (2006) and adopted here may be explained by scarce vegetation and thick vadose zone with almost constant moisture (Gonçalvès et al., 2013) in arid and semi-arid domain and therefore rather limited differences in controlling factors except rainfall. Such linear relation is also suggested here by punctual or regional scale estimates of the recharge (Figure 7).

The observed linear relationship between AAR and recharge suggests, to the first order and for the arid domain considered here, a scale invariance of the recharge. Indeed, the local linear relation $R = a * \mathrm{AAR} + b$ leads to a domain averaged relation $\overline{R} = a * \overline{\mathrm{AAR}} + b$ with $\overline{\mathrm{AAR}}$ and $\overline{R}$ the domain-averaged values of AAR and R. Therefore, the values obtained at different scales and with different methods should align on the linear regression shown in Figure 7. Several domain averaged values are reported in Figure 7, ascertained either using global mass-balance equations combined with Satellite gravity data or by regional hydrogeological modeling for different aquifers of the Saharan belt (Baba Sy, 2005; Gonçalvès et al., 2021; Heinl & Brinkmann, 1989; Mohamed & Gonçalvès, 2021; Mohamed et al., 2017; Pizzi & Sartori, 1984). Additional local scale estimates are also shown (Edmunds, 2001; Fontes et al., 1986; Yermani et al., 2009), which were obtained using geochemical profiles (chlorine and stable isotopes of water) in the unsaturated zone in locations away from wadis. Therefore, they refer to diffuse recharge or discharge, whereas here we identified total recharge. Despite variable scales and acquisition methods, these data are in good agreement with the global linear relation determined using the approach described in this study (Figure 7).

Turning now to the precise comparison between radiocarbon-derived recharge estimates and the values obtained by independent methods, we focus on the NWSAS and the Djeffara plain. Here, we derived from ^{14}C data an average recharge of 1.1 ± 1.5 km^3 yr^{-1} for the NWSAS and 0.17 ± 0.1 km^3 yr^{-1} for the Djeffara plain. For the NWSAS, global (CI and CT) recharge values of 1.0 ± 0.2 km^3 yr^{-1} were calculated using a regional groundwater flow model by Baba Sy (2005), and a value at 1.4 ± 0.9 km^3 yr^{-1} was estimated using an overall mass balance and Gravity Recovery and Climate Experiment (GRACE) Satellite gravity data by Gonçalvès et al. (2013) recently updated at 1.1 ± 0.3 km^3 yr^{-1} using a longer time-series by Mohamed and Gonçalvès (2021). A value of the recharge at 0.33 km^3 yr^{-1} (6.85 mm yr^{-1} over the surface area of 48,000 km^2) was obtained for the Djeffara (OSS, 2006). However, this value corresponds to both natural and artificial (irrigation return flow) recharge. Furthermore, a recent estimation of recharge of the Djeffara at 4.3 ± 2.7 mm yr^{-1} was obtained by Gonçalvès et al. (2021) using GRACE data. Overall, the different approaches led to consistent values for the regional recharge of these two Saharan aquifer systems.

6. Conclusions

In this study, we interpreted 25 radiocarbon data from the main Saharan aquifers by considering the temporal evolution of the recharge rate over the last 40 Kyr in Saharan and Mediterranean aquifers. For this purpose, we extended the two-dimensional hydrodynamic age model of Vogel (1967) for unconfined aquifers, in order to account for time varying recharge and we developed two alternative expressions: (a) an approximate TS analytical model and (b) a PSS model for highly reactive aquifers. Despite some simplifications (constant saturated thickness, perfect vertical mixing), the PSS and TS analytical models developed here represent convenient alternative approaches to more complex numerical solutions and related particle tracking calculations. The consistency of our approach was tested by estimating the recharge of Saharan aquifer systems for which independent estimates of the present recharge were available (regional average values). We selected radiocarbon data by retaining only groundwater samples collected within the

same free-surface aquifer formation, on a clearly identified streamline receiving no contribution of deep groundwater inflow (discharge area of confined parts) or local recharge. The application of PSS and TS expressions to the NWSAS and the Djeffara aquifers led to a present recharge ranging from 0.2 ± 1.7 to 4.5 ± 3.2 mm yr^{-1}, with a domain-averaged value of 1.6 ± 2.3 mm yr^{-1} (1.1 ± 1.5 km^3 yr^{-1}) for NWSAS and 3.5 ± 2.3 mm yr^{-1} (0.17 ± 0.1 km^3 yr^{-1}) for the Djeffara obtained with a linear relation between AAR and recharge rate estimates at different outcrops. These values are in good agreement with the available regional-scale estimates obtained from hydrogeological modeling (Baba Sy, 2005; OSS, 2006) or geophysical methods (satellite-derived values; Mohamed & Gonçalvès, 2021). This expression may thus be used for recharge prediction in Saharan aquifers, which is fundamental information for the management of groundwater systems. Given that most of the recharge error is due to the uncertainty associated with the ^{14}C activity data (Aggarwal et al., 2014), new sampling campaigns in Saharan aquifers using up-to-date sampling (e.g., stainless-steel ampoules) and analytical (AMS) techniques could improve the accuracy of the recharge estimates and the derived linear regression. Sampling strategies for this future field campaigns should be designed according to the available interpretation model. For instance, if no 3D-hydrogeological model is available, a field campaign focusing on a few streamlines and using the solution developed here should be considered.

Appendix A: Identification of the Models

Appendix A1. TS Model

Free-surface aquifers satisfy the continuity equation which is written in 2D:

$$\mathrm{div}\left(\vec{q}\right) = \frac{\partial q_x}{\partial x} + \frac{\partial q_z}{\partial z} = 0 \tag{A1}$$

with a boundary condition at the free-surface which is written (Bear, 1979):

$$K_x \frac{\partial h}{\partial x}\frac{\partial \zeta}{\partial x} - K_z \frac{\partial h}{\partial z} + R = S_y \frac{\partial \zeta}{\partial t} \tag{A2}$$

where q_x and q_z and K_x and K_z are the specific discharge (m s^{-1}) and the hydraulic conductivities along the x and z directions (m), R is the recharge (m s^{-1}), $\zeta(x,t)$ is the free-surface elevation (m), $h(x,z,t)$ is the hydraulic head (m), and S_y is the dimensionless specific yield. We solved Equations A1 and A2 to identify practical-use analytical expressions for q_x and q_z which facilitate particle-tracking calculations. For this purpose, Equation A2 was solved for $\zeta(x,t)$ using a finite difference explicit scheme which requires small time step (about 1 year). We verified that the first term on the left-hand side of Equation A2 is negligible due to low hydraulic (phreatic surface) gradients, especially in the arid regions studied here which are characterized by a few mm of recharge per year. Equation A1 was then solved by introducing Darcy's law:

$$\begin{cases} q_x = -K_x \dfrac{\partial h}{\partial x} \\ q_z = -K_z \dfrac{\partial h}{\partial z} \end{cases} \tag{A3}$$

for $h(x,z,t)$ using a finite differences implicit scheme. Here, we assumed an isotropic permeability field ($K_x = K_z$) considering that the permeability field influences the hydraulic head gradients while q_x and q_z, which are the components sought after here, are mostly controlled by R as suggested by steady-state expressions.

Equations A1–A3 were solved for a base case using $L = 100$ km, $H = 100$ m, $R = 1$ mm yr^{-1}, $K_x = 5 \times 10^{-4}$ m s^{-1}, and $S_y = 0.05$ (plausible values for the CT aquifer). However, the outputs are presented here using non-dimensional variables since the results can be generalized for various dimensions and characteristic times. In this numerical base case, we considered an instantaneous increase in the recharge from 0 to R at $t = 0$ together with $h(x,t = 0) = H$ as the initial condition, and the following boundary conditions: $h = H$ at $x = L$ and $q_x = 0$ at $x = 0$. Assuming $T \approx K_x H$, that is, an almost constant saturated thickness similarly to

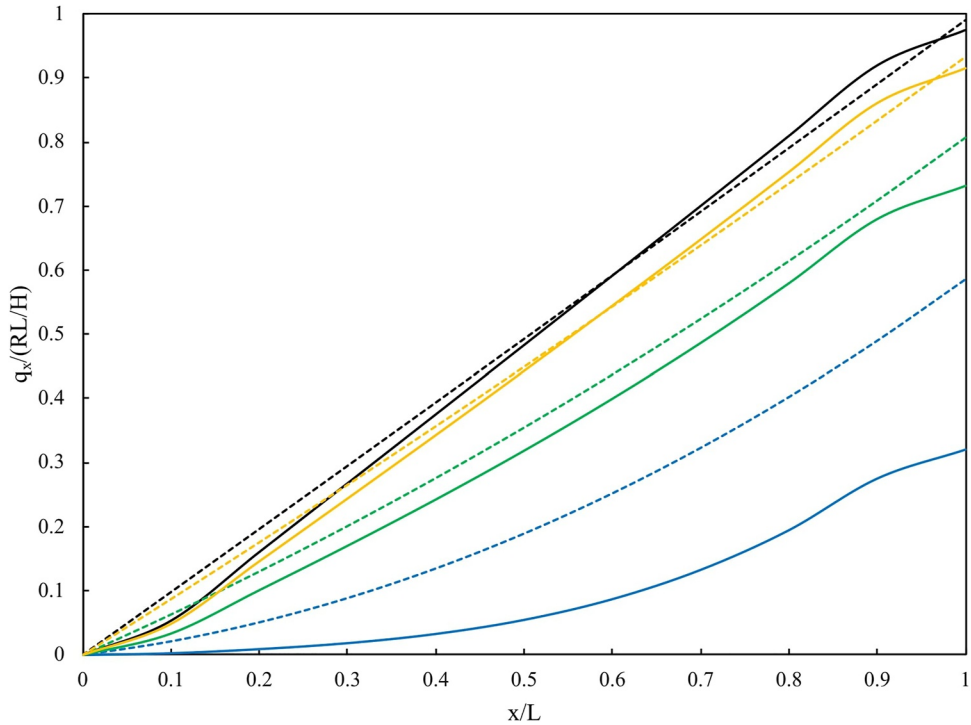

Figure A1. Comparison between numerical solution (plain lines) and pseudo-analytical solution Equation A4 (dashed lines) for non-dimensional $q_x/(RL/H)$ where RL/H is the maximum value at steady-state value at times 0.1τ (blue), 0.5τ (green), 1τ (yellow), and 2τ (black).

Vogel (1967), the following approximate expressions satisfying the continuity equation (Equation A2) and the boundary conditions were identified:

$$q_x\left(x,t\right)=\frac{R}{H}\left[\exp\left(-\frac{2t}{\tau}\right)\frac{x^2}{2L}+\left(1-\exp\left(-\frac{2t}{\tau}\right)\right)x\right] \tag{A4}$$

and:

$$q_z\left(x,z,t\right)=-\frac{R}{H}\left[\exp\left(-\frac{2t}{\tau}\right)\frac{x}{L}+\left(1-\exp\left(-\frac{2t}{\tau}\right)\right)\right]z \tag{A5}$$

We verified here that the vertical component of the specific discharge q_z is linearly dependent on z with $q_z=0$ at $z=0$. Therefore $q_z(x,z,t)$ is fully determined by its maximum value at the free-surface $q_z^{FS}(x,t)$ which is thus dependent on the x location in TS. The comparison between the numerical and approximate analytical expression for q_x (using $qx/(RL/H)$) and q_z (using q_z^{FS}/R) is depicted in Figures A1 and A2. Equations A4 and A5 produce an instantaneous rise in q_x and q_z when R becomes positive which explains the initial overestimation shown in Figures A1 and A2. However, despite this relatively large error at the very early times of the TS, the expected overall error in a particle tracking model using these expressions is small. Indeed, using the approximate analytical expression for q_x and q_z leads to an average specific discharge and thus total position error for a water particle with respect to the numerical solution which is less than 0.3% of L (300 m for $L=100$ km) in x and less than 1% of H (1 m for $H=100$ m) in z assuming $\omega_c=0.1$ and $R=1$ mm yr^{-1}. Note that this error which is likely in the same order as the numerical error is acquired during the transient period (1 or 2τ see below) since the solution is exact at steady state. Figure A3 illustrates the reactivity of the unconfined aquifer based on the z component q_z calculated using Equation A5. After 1τ, the difference with the steady-state is only about 5%. More importantly for exploitation of the model, for low characteristic time values, it can be seen that the velocity adjusts very rapidly in comparison to the time scale for Holocene climatic variations, that is, 5 Kyr. This could lead to neglecting the TS and postulating a

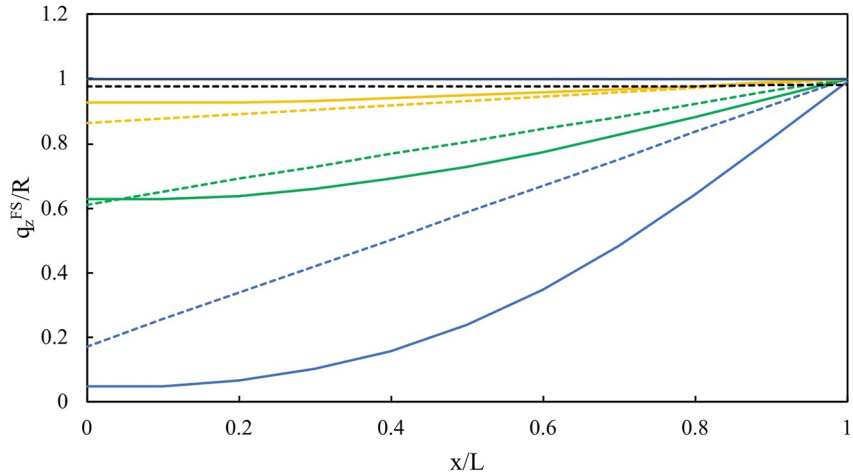

Figure A2. Comparison between numerical solution (plain lines) and pseudo-analytical solution Equation A5 (dashed lines) for q_z using the maximum value q_z^{FS} at times 0.1τ (blue), 0.5τ (green), 1τ (yellow), and 2τ (black).

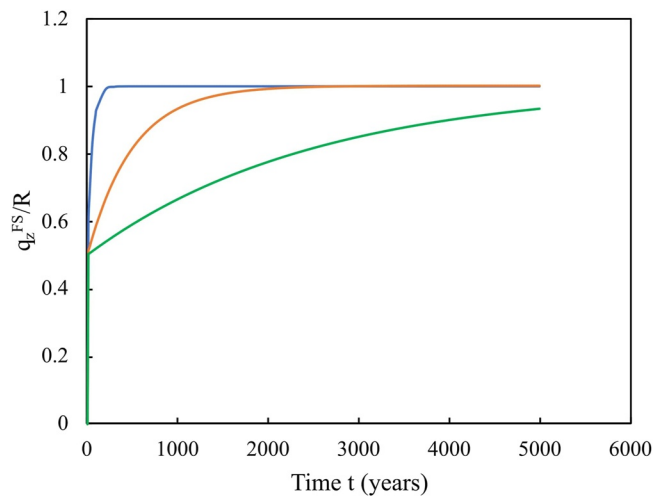

Figure A3. Averaged value over the distance x of q_z^{FS} as a function of time for different values of τ: 100 years (blue), 1,000 yearsr (orange), and 5,000 years (green).

steady-state behavior for particle tracking calculations (see Appendix A2). For example, assuming such a steady state for an aquifer with $\tau = 1{,}000$ years leads to a maximum error in the z position of a water particle of 2.25 m per 1 mm yr^{-1} of recharge while this maximum error is 3.5 m for $\tau = 1{,}500$ years.

Appendix A2. PSS Model

For very reactive aquifers (high diffusivity, small L, or a combination of both conditions), that is, for small characteristic times τ, a succession of steady states separated by very short intermediate TS occurs. Therefore, the square wave time function for the temporally varying recharge produces a velocity field that adjusts almost instantaneously for $\tau << 5$ Kyr (see Appendix A1). The TS can then be largely neglected, and Vogel's (1967) solution can be extended in a pseudo-steady state approach. In this case q_z depends only on z and is expressed using the square wave scenario for the recharge considered here:

$$q_z = \frac{R(t)}{H} z \tag{A6}$$

with (see Figure 3 for time notations):

$$\begin{cases} R(t) = \alpha_1 R & if\ 0 \le t < t_1 \\ R(t) = \alpha_2 R & if\ t_1 \le t < t_2 \\ R(t) = R & if\ t_2 \le t < t_3 \end{cases} \tag{A7}$$

Introducing Equation A6 divided by ω to obtain v_z into the infinitesimal fluid motion equation $v_z dt = dz$ for the z component and upon integration between the time t when the fluid particle is at the free-surface (at $z = H$) and present-day t_3 (particle at location z) gives:

$$\int_t^{t_3} R(t)\,d(t) = -\int_H^z \omega H \frac{dz}{z} \tag{A8}$$

Equation A8 accounting for Equation A7 gives:

$$\begin{cases} \frac{\alpha_1 R}{H\omega}(t_1 - t) + \frac{\alpha_2 R}{H\omega}(t_2 - t_1) + \frac{R}{H\omega}(t_3 - t_2) = ln\left(\frac{H}{z}\right) & if\ 0 \le t < t_1 \\ \frac{\alpha_2 R}{H\omega}(t_2 - t) + \frac{R}{H\omega}(t_3 - t_2) = ln\left(\frac{H}{z}\right) & if\ t_1 \le t < t_2 \\ \frac{R}{H\omega}(t_3 - t) = ln\left(\frac{H}{z}\right) & if\ t_2 \le t < t_3 \end{cases} \tag{A9}$$

Using Equation 15 and the groundwater age $t' = t_3 - t$, the Equation A9 can be converted from *(z,t)* to *(A,z)* resulting in a system of piece-wise power law relations *A(z)* bounded by the z coordinates corresponding to groundwater ages of 40 ka BP (z_0), 10 ka BP (z_1), and 5 ka BP (z_2) which is written:

$$\begin{cases} \frac{A}{A_0} = \left(\frac{z}{H}\right)^{\beta_1} & \text{if } z_2 < z \le H \\ \frac{A}{A_0} = \beta_2 \left(\frac{z}{H}\right)^{\beta_3} & \text{if } z_1 < z \le z_2 \\ \frac{A}{A_0} = \beta_4 \left(\frac{z}{H}\right)^{\beta_5} & \text{if } z_0 < z \le z_1 \\ \frac{A}{A_0} = 0 & \text{if } z \le z_0 \end{cases} \tag{A10}$$

where

$$\beta_1 = \frac{H\omega\lambda}{R}; \beta_3 = \frac{H\omega\lambda}{\alpha_2 R}; \beta_5 = \frac{H\omega\lambda}{\alpha_1 R} \tag{A11}$$

$$\beta_2 = \exp\left(-\frac{\lambda}{\alpha_2}(t_3 - t_2)(\alpha_2 - 1)\right) \tag{A12}$$

$$\beta_4 = \exp\left(\lambda(t_1 - t_3) + \frac{\lambda\alpha_2}{\alpha_1}(t_2 - t_1) + \frac{\lambda}{\alpha_1}(t_3 - t_2)\right) \tag{A13}$$

$$z_0 = H.\exp\left(-\frac{\alpha_1 R t_1}{\omega H} - \frac{\alpha_2 R}{\omega H}(t_2 - t_1) - \frac{R}{\omega H}(t_3 - t_2)\right) \tag{A14}$$

$$z_1 = H.\exp\left(-\frac{\alpha_2 R}{\omega H}(t_2 - t_1) - \frac{R}{\omega H}(t_3 - t_2)\right) \tag{A15}$$

$$z_2 = H.\exp\left(-\frac{R}{\omega H}\left(t_3 - t_2\right)\right) \quad \text{(A16)}$$

Data Availability Statement

Data sets for this research are available through: Aggarwal et al., 2014; Alder & Hostetler, 2015; Baba Sy, 2005; Blanchet et al., 2021; Claussen et al., 2013; Conaway et al., 2018; Edmunds, 2001; ERESS, 1972; Fontes et al., 1986; Gelhar et al., 1992; Gonçalvès et al., 2013, 2021; Gonfiantini et al., 1974; Guendouz et al., 2003; Hadj Ammar, 2016; Hadj Ammar et al., 2014, 2020; Heinl & Brinkmann, 1989; Hopcroft et al., 2017; Kageyama et al., 2013; Larrasoaña et al., 2013; Mohamed & Gonçalvès, 2021; Mohamed et al., 2017; Nakata et al., 2016; OSS, 2003, 2006; Pallas, 1972, as cited in Swezey, 1999; Petersen et al., 2014, 2018; Pizzi & Sartori, 1984; Rightmire & Hanshaw, 1973; Srdoč et al., 1982; Tierney et al., 2017; Yermani et al., 2009; Yokochi et al., 2018; Zouari et al., 2011. No new data were provided in this article.

Acknowledgments
This study has been supported by the Labex OT-Med project of the French program "Investissement d'Avenir." The three anonymous reviewers and the Editors are acknowledged for their relevant comments which largely improved the manuscript.

References

Abid, K., Dulinski, M., Ammar, F. H., Rozanski, K., & Zouari, K. (2012). Deciphering interaction of regional aquifers in Southern Tunisia using hydrochemistry and isotopic tools. *Applied Geochemistry*, *27*(1), 44–55. https://doi.org/10.1016/j.apgeochem.2011.08.015

Abrantes, F., Voelker, A., Helga, L., Sierro, F. J., Naughton, F., Rodrigues, T., et al. (2012). Paleoclimate Variability in the Mediterranean Region. In: *The climate of the Mediterranean region* (pp. 1–86). Elsevier. https://doi.org/10.1016/B978-0-12-416042-2.00001-X

Aggarwal, P. K., Araguas-Araguas, L., Choudhry, M., van Duren, M., & Froehlich, K. (2014). Lower groundwater ^{14}C Age by atmospheric CO_2 uptake during sampling and analysis. *Groundwater*, *52*(1), 20–24. https://doi.org/10.1111/gwat.12110

Alder, J. R., & Hostetler, S. W. (2015). Global climate simulations at 3000-year intervals for the last 21 000 years with the GENMOM coupled atmosphere-ocean model. *Climate of the Past*, *11*(3), 449–471. https://doi.org/10.5194/cp-11-449-2015

Baba Sy, M. (2005). *Recharge et paléorecharge du Système Aquifère du Sahara Septentrional (PhD Thesis)*. Université of Tunisia.

Bear, J. (1979). *Hydraulics of groundwater (McGraw-Hill series in water resources and environmental engineering)*. McGraw-Hill.

Bear, J., Cheng, A. H. D., Batu, V., Chen, C., Kuang, X., & Jimmy Jiao, J. (2010). Methods to derive the differential equation of the free surface boundary. *Groundwater*, *48*(4), 486–493. https://doi.org/10.1111/j.1745-6584.2010.00711.x

Bethke, C. M., & Johnson, T. M. (2008). Groundwater age and groundwater age dating. *Annual Review of Earth and Planetary Sciences*, *36*(1), 121–152. https://doi.org/10.1146/annurev.earth.36.031207.124210

Blanchet, C. L., Osborne, A. H., Tjallingii, R., Ehrmann, W., Friedrich, T., Timmermann, A., et al. (2021). Drivers of river reactivation in North Africa during the last glacial cycle. *Nature Geoscience*, *14*(2), 97–103. https://doi.org/10.1038/s41561-020-00671-3

Böhlke, J.-K. (2002). Groundwater recharge and agricultural contamination. *Hydrogeology Journal*, *10*(1), 153–179. https://doi.org/10.1007/s10040-001-0183-3

Bredenkamp, D. B., & Vogel, J. C. (1970). Study of a dolomitic aquifer with carbon-14 and tritium. Paper presented at the Isotope Hydrology 1970, Proceedings of an IAEA Symposium, Vienna. Retrieved from http://inis.iaea.org/Search/search.aspx?orig_q=RN:38054536

Cartwright, I., Cendón, D., Currell, M., & Meredith, K. (2017). A review of radioactive isotopes and other residence time tracers in understanding groundwater recharge: Possibilities, challenges, and limitations. *Journal of Hydrology*, *555*, 797–811. https://doi.org/10.1016/j.jhydrol.2017.10.053

Cartwright, I., Currell, M. J., Cendón, D. I., & Meredith, K. T. (2020). A review of the use of radiocarbon to estimate groundwater residence times in semi-arid and arid areas. *Journal of Hydrology*, *580*, 124247. https://doi.org/10.1016/j.jhydrol.2019.124247

Clark, I., & Fritz, P. (1997). *Environmental isotopes in hydrology*. Lewis Publishers.

Claussen, M., Bathiany, S., Brovkin, V., & Kleinen, T. (2013). Simulated climate–vegetation interaction in semi-arid regions affected by plant diversity. *Nature Geoscience*, *6*(11), 954–958. https://doi.org/10.1038/ngeo1962

Collins, J. A., Prange, M., Caley, T., Gimeno, L., Beckmann, B., Mulitza, S., et al. (2017). Rapid termination of the African Humid Period triggered by northern high-latitude cooling. *Nature Communications*, *8*(1), 1372. https://doi.org/10.1038/s41467-017-01454-y

Combourieu Nebout, N., Peyron, O., Dormoy, I., Desprat, S., Beaudouin, C., Kotthoff, U., & Marret, F. (2009). Rapid climatic variability in the west Mediterranean during the last 25 000 years from high resolution pollen data. *Climate of the Past*, *5*(3), 503–521. https://doi.org/10.5194/cp-5-503-2009

Conaway, C. H., Walvoord, M. A., Thomas, R. B., Green, C. T., Baker, R. J., Thordsen, J. J., et al. (2018). Unsaturated zone CO2, CH4, and δ13C-CO2 at an arid region low-level radioactive waste disposal site. *Vadose Zone Journal*, *17*(1), 170200. https://doi.org/10.2136/vzj2017.11.0200

Cook, P. G., & Böhlke, J.-K. (2000). Determining timescales for groundwater flow and solute transport. In P. G. Cook & A. L. Herczeg (Eds.), *Environmental tracers in subsurface hydrology* (pp. 1–30). Springer. https://doi.org/10.1007/978-1-4615-4557-6_1

Cook, P. G., Edmunds, W. M., & Gaye, C. B. (1992). Estimating paleorecharge and paleoclimate from unsaturated zone profiles. *Water Resources Research*, *28*(10), 2721–2731. https://doi.org/10.1029/92WR01298

Cook, P. G., Jolly, I. D., Leaney, F. W., Walker, G. R., Allan, G. L., Fifield, L. K., & Allison, G. B. (1994). Unsaturated zone tritium and chlorine 36 profiles from southern Australia: Their use as tracers of soil water movement. *Water Resources Research*, *30*(6), 1709–1719. https://doi.org/10.1029/94WR00161

Delin, G. N., Healy, R. W., Landon, M. K., & Böhlke, J. K. (2000). Effects of topography and soil properties on recharge at two sites in an agricultural field. *Journal of the American Water Resources Association*, *36*(6), 1401–1416. https://doi.org/10.1111/j.1752-1688.2000.tb05735.x

Delin, G. N., Healy, R. W., Lorenz, D. L., & Nimmo, J. R. (2007). Comparison of local- to regional-scale estimates of ground-water recharge in Minnesota, USA. *Journal of Hydrology*, *334*(1–2), 231–249.

deMenocal, P., Ortiz, J., Guilderson, T., Adkins, J., Sarnthein, M., Baker, L., & Yarusinsky, M. (2000). Abrupt onset and termination of the African Humid Period: Rapid climate responses to gradual insolation forcing. *Quaternary Science Reviews*, *19*(1), 347–361. https://doi.org/10.1016/S0277-3791(99)00081-5

Desprat, S., Combourieu-Nebout, N., Essallami, L., Sicre, M. A., Dormoy, I., Peyron, O., et al. (2013). Deglacial and Holocene vegetation and climatic changes in the southern Central Mediterranean from a direct land–sea correlation. *Climate of the Past*, *9*(2), 767–787. https://doi.org/10.5194/cp-9-767-2013

Dupuit, J. (1863). *Etudes théoriques et pratiques sur le mouvement des eaux dans les canaux découverts et à travers les terrains perméables* (2nd ed.). Dunod.

Edmunds, W. M. (2001). *Investigation of the unsaturated zone in semi-arid regions using isotopic and chemical methods and applications to water resource problems*. Retrieved from https://www.osti.gov/etdeweb/biblio/20224652

Edmunds, W. M., Guendouz, A. H., Mamou, A., Moulla, A., Shand, P., & Zouari, K. (2003). Groundwater evolution in the Continental Intercalaire aquifer of southern Algeria and Tunisia: Trace element and isotopic indicators. *Applied Geochemistry*, *18*(6), 805–822. https://doi.org/10.1016/S0883-2927(02)00189-0

Edmunds, W. M., & Wright, E. P. (1979). Groundwater recharge and palaeoclimate in the Sirte and Kufra basins, Libya. *Journal of Hydrology*, *40*(3), 215–241. https://doi.org/10.1016/0022-1694(79)90032-5

Eichinger, L. (1983). A contribution to the interpretation of (super 14) C groundwater ages considering the example of a partially confirmed sandstone aquifer. *Radiocarbon*, *25*(2), 347–356. https://doi.org/10.1017/s0033822200005634

ERESS. (1972). *Etude des ressources en eau du Sahara Septentrional. La nappe du continentale intercalaire. Modèle mathématique. Plaquette 2 (Rapport final)*. UNESCO.

Fontes, J. C., & Garnier, J.-M. (1979). Determination of the initial ^{14}C activity of the total dissolved carbon: A review of the existing models and a new approach. *Water Resources Research*, *15*(2), 399–413. https://doi.org/10.1029/WR015i002p00399

Fontes, J. C., Gasse, F., Callot, Y., Plaziat, J.-C., Carbonel, P., Dupeuble, P. A., & Kaczmarska, I. (1985). Freshwater to marine-like environments from Holocene lakes in northern Sahara. *Nature*, *317*, 608–610. https://doi.org/10.1038/317608a0

Fontes, J. C., Yousfi, M., & Allison, G. B. (1986). Estimation of long-term, diffuse groundwater discharge in the northern Sahara using stable isotope profiles in soil water. *Journal of Hydrology*, *86*(3), 315–327. https://doi.org/10.1016/0022-1694(86)90170-8

Gasse, F. (2000). Hydrological changes in the African tropics since the Last Glacial Maximum. *Quaternary Science Reviews*, *19*(1), 189–211. https://doi.org/10.1016/S0277-3791(99)00061-X

Gelhar, L. W., Welty, C., & Rehfeldt, K. R. (1992). A critical review of data on field-scale dispersion in aquifers. *Water Resources Research*, *28*(7), 1955–1974. https://doi.org/10.1029/92WR00607

Gerber, C., Purtschert, R., Hunkeler, D., Hug, R., & Sültenfuss, J. (2018). Using environmental tracers to determine the relative importance of travel times in the unsaturated and saturated zones for the delay of nitrate reduction measures. *Journal of Hydrology*, *561*, 250–266. https://doi.org/10.1016/j.jhydrol.2018.03.043

Gonfiantini, R., Conrad, G., FontesSauzay, J.-C. G., & Payne, B. (1974). Etude isotopique de la nappe du continental intercalaire et de ses relations avec les autres nappes du Sahara Septentrional. *Isotope Techniques in Groundwater Hydrology*, *1*, 227–241.

Gonçalvès, J., Deschamps, P., Hamelin, B., Vallet-Coulomb, C., Petersen, J., & Chekireb, A. (2020). Revisiting recharge and sustainability of the North-Western Sahara aquifers. *Regional Environmental Change*, *20*(2), 47. https://doi.org/10.1007/s10113-020-01627-4

Gonçalvès, J., Petersen, J., Deschamps, P., Hamelin, B., & Baba-Sy, O. (2013). Quantifying the modern recharge of the "fossil" Sahara aquifers. *Geophysical Research Letters*, *40*(11), 2673–2678. https://doi.org/10.1002/grl.50478

Gonçalvès, J., Séraphin, P., Stieglitz, T., Chekireb, A., Hamelin, B., & Deschamps, P. (2021). Coastal aquifer recharge and groundwater-seawater exchanges using downscaled GRACE data: Case study of the Djeffara plain (Libya-Tunisia). *Comptes Rendus Geoscience*.

Gonçalvès, J., Vallet-Coulomb, C., Petersen, J., Hamelin, B., & Deschamps, P. (2015). Declining water budget in a deep regional aquifer assessed by geostatistical simulations of stable isotopes: Case study of the Saharan "Continental Intercalaire". *Journal of Hydrology*, *531*, 821–829. https://doi.org/10.1016/j.jhydrol.2015.10.044

Grant, K. M., Rohling, E. J., Westerhold, T., Zabel, M., Heslop, D., Konijnendijk, T., & Lourens, L. (2017). A 3 million year index for North African humidity/aridity and the implication of potential pan-African Humid periods. *Quaternary Science Reviews*, *171*, 100–118. https://doi.org/10.1016/j.quascirev.2017.07.005

Guendouz, A., Moulla, A. S., Edmunds, W. M., Zouari, K., Shand, P., & Mamou, A. (2003). Hydrogeochemical and isotopic evolution of water in the Complexe Terminal aquifer in the Algerian Sahara. *Hydrogeology Journal*, *11*(4), 483–495. https://doi.org/10.1007/s10040-003-0263-7

Hadj Ammar, F. (2016). *Caractérisation des eaux de l'aquifère du complexe terminal: Approche multi-isotopiques ($^{234}U/^{238}U$, ^{36}Cl, ^{14}C, $\delta^{18}O$, $\delta^{2}H$) (These de doctorat)*. Aix-Marseille Université. Retrieved from https://www.theses.fr/2016AIXM4384

Hadj Ammar, F., Chkir, N., Zouari, K., Hamelin, B., Deschamps, P., & Aigoun, A. (2014). Hydro-geochemical processes in the Complexe Terminal aquifer of southern Tunisia: An integrated investigation based on geochemical and multivariate statistical methods. *Journal of African Earth Sciences*, *100*, 81–95. https://doi.org/10.1016/j.jafrearsci.2014.06.015

Hadj Ammar, F., Deschamps, P., Chkir, N., Zouari, K., Agoune, A., & Hamelin, B. (2020). Uranium isotopes as tracers of groundwater evolution in the Complexe Terminal aquifer of southern Tunisia. *Quaternary International*, *547*, 33–49. https://doi.org/10.1016/j.quaint.2020.01.024

Han, L. F., & Plummer, L. N. (2016). A review of single-sample-based models and other approaches for radiocarbon dating of dissolved inorganic carbon in groundwater. *Earth-Science Reviews*, *152*, 119–142. https://doi.org/10.1016/j.earscirev.2015.11.004

Harrington, G. A., Cook, P. G., & Herczeg, A. L. (2002). Spatial and temporal variability of ground water recharge in central Australia: A tracer approach. *Ground Water*, *40*(5), 518–527. https://doi.org/10.1111/j.1745-6584.2002.tb02536.x

Heinl, M., & Brinkmann, P. J. (1989). A groundwater model of the Nubian aquifer system. *Hydrological Sciences Journal*, *34*(4), 425–447. https://doi.org/10.1080/02626668909491350

Hély, C., Lézine, A.-M., & Contributors, A. P. D. (2014). Holocene changes in African vegetation: Tradeoff between climate and water availability. *Climate of the Past*, *10*(2), 681–686. https://doi.org/10.5194/cp-10-681-2014

Hoelzmann, P., Gasse, F., Dupont, L. M., Salzmann, U., Staubwasser, M., Leuschner, D. C., & Sirocko, F. (2004). Palaeoenvironmental changes in the arid and sub arid belt (Sahara-Sahel-Arabian Peninsula) from 150 kyr to present. In R. W. Battarbee, F. Gasse, & C. E. Stickley (Eds.), *Past climate variability through Europe and Africa* (pp. 219–256). Springer. https://doi.org/10.1007/978-1-4020-2121-3_12

Hoffmann, D. L., Rogerson, M., Spötl, C., Luetscher, M., Vance, D., Osborne, A. H., et al. (2016). Timing and causes of North African wet phases during the last glacial period and implications for modern human migration. *Scientific Reports*, *6*(1), 36367. https://doi.org/10.1038/srep36367

Hopcroft, P. O., Valdes, P. J., Harper, A. B., & Beerling, D. J. (2017). Multi vegetation model evaluation of the Green Sahara climate regime: Rainfall supporting a Green Sahara. *Geophysical Research Letters*, *44*(13), 6804–6813. https://doi.org/10.1002/2017GL073740

Irvine, D., Wood, C., Cartwright, I., & Oliver, T. (2021). Depth to water table correction for initial carbon-14 activities in groundwater mean residence time estimation. *Hydrology and Earth System Sciences*, *25*, 5415–5424. https://doi.org/10.5194/hess-2021-276

Kageyama, M., Braconnot, P., Bopp, L., Caubel, A., Foujols, M. A., Guilyardi, E., et al. (2013). Mid-Holocene and Last Glacial Maximum climate simulations with the IPSL model-part I: Comparing IPSL_CM5A to IPSL_CM4. *Climate Dynamics*, *40*(9–10), 2447–2468. https://doi.org/10.1007/s00382-012-1488-8

Kamai, T., & Assouline, S. (2018). Evaporation from deep aquifers in arid regions: Analytical model for combined liquid and vapor water fluxes. *Water Resources Research*, *54*(7), 4805–4822. https://doi.org/10.1029/2018WR023030

Keese, K. E., Scanlon, B. R., & Reedy, R. C. (2005). Assessing controls on diffuse groundwater recharge using unsaturated flow modeling. *Water Resources Research*, *41*(6). https://doi.org/10.1029/2004WR003841

Kutzbach, J. E., Chen, G., Cheng, H., Edwards, R. L., & Liu, Z. (2014). Potential role of winter rainfall in explaining increased moisture in the Mediterranean and Middle East during periods of maximum orbitally-forced insolation seasonality. *Climate Dynamics*, *42*(3–4), 1079–1095. https://doi.org/10.1007/s00382-013-1692-1

Larrasoaña, J. C., Roberts, A. P., & Rohling, E. J. (2013). Dynamics of Green Sahara periods and their role in Hominin evolution. *PLoS One*, *8*(10), e76514. https://doi.org/10.1371/journal.pone.0076514

Lasagna, M., & De Luca, D. A. (2016). The use of multilevel sampling techniques for determining shallow aquifer nitrate profiles. *Environmental Science and Pollution Research*, *23*(20), 20431–20448. https://doi.org/10.1007/s11356-016-7264-2

Le Gal La Salle, C., Marlin, C., Leduc, C., Taupin, J. D., Massault, M., & Favreau, G. (2001). Renewal rate estimation of groundwater based on radioactive tracers (3H, 14C) in an unconfined aquifer in a semi-arid area, Iullemeden Basin, Niger. *Journal of Hydrology*, *254*(1), 145–156. https://doi.org/10.1016/S0022-1694(01)00491-7

Leaney, F. W., & Allison, G. B. (1986). Carbon-14 and stable isotope data for an area in the Murray Basin: Its use in estimating recharge. *Journal of Hydrology*, *88*(1), 129–145. https://doi.org/10.1016/0022-1694(86)90201-5

Lécuyer, C., Lézine, A.-M., Fourel, F., Gasse, F., Sylvestre, F., Pailles, C., et al. (2016). I-n-Atei palaeolake documents past environmental changes in central Sahara at the time of the "Green Sahara": Charcoal, carbon isotope and diatom records. *Palaeogeography, Palaeoclimatology, Palaeoecology*, *441*, 834–844. https://doi.org/10.1016/j.palaeo.2015.10.032

Lekula, M., & Lubczynski, M. W. (2019). Use of remote sensing and long-term in-situ time-series data in an integrated hydrological model of the Central Kalahari Basin, Southern Africa. *Hydrogeology Journal*, *27*(5), 1541–1562. https://doi.org/10.1007/s10040-019-01954-9

Leray, S., de Dreuzy, J.-R., Bour, O., Labasque, T., & Aquilina, L. (2012). Contribution of age data to the characterization of complex aquifers. *Journal of Hydrology*, *464*(465), 54–68. https://doi.org/10.1016/j.jhydrol.2012.06.052

Lézine, A.-M., Hély, C., Grenier, C., Braconnot, P., & Krinner, G. (2011). Sahara and Sahel vulnerability to climate changes, lessons from Holocene hydrological data. *Quaternary Science Reviews*, *30*(21), 3001–3012. https://doi.org/10.1016/j.quascirev.2011.07.006

MacDonald, A. M., Bonsor, H. C., Dochartaigh, B. É. Ó., & Taylor, R. G. (2012). Quantitative maps of groundwater resources in Africa. *Environmental Research Letters*, *7*(2), 024009. https://doi.org/10.1088/1748-9326/7/2/024009

MacDonald, A. M., Lark, R. M., Taylor, R. G., Abiye, T., Fallas, H. C., Favreau, G., et al. (2021). Mapping groundwater recharge in Africa from ground observations and implications for water security. *Environmental Research Letters*, *16*(3), 034012. https://doi.org/10.1088/1748-9326/abd661

Marsily, G. de (1986). *Quantitative hydrogeology: Groundwater hydrology for engineers*. Academic Press.

Massoudieh, A. (2013). Inference of long-term groundwater flow transience using environmental tracers: A theoretical approach. *Water Resources Research*, *49*(12), 8039–8052. https://doi.org/10.1002/2013WR014548

McCallum, J. L., Cook, P. G., & Simmons, C. T. (2015). Limitations of the use of environmental tracers to infer groundwater age. *Groundwater*, *53*(S1), 56–70. https://doi.org/10.1111/gwat.12237

McCallum, J. L., Dogramaci, S., Bai, A., Cook, P. G., Engdahl, N. B., Simmons, C. T., et al. (2020). Assessing temporal changes in groundwater recharge using spatial variations in groundwater ages. *Water Resources Research*, *56*(8). https://doi.org/10.1029/2020WR027240

McMahon, P. B., Plummer, L. N., Böhlke, J. K., Shapiro, S. D., & Hinkle, S. R. (2011). A comparison of recharge rates in aquifers of the United States based on groundwater-age data. *Hydrogeology Journal*, *19*(4), 779–800. https://doi.org/10.1007/s10040-011-0722-5

Mohamed, A., & Gonçalvès, J. (2021). Hydro-geophysical monitoring of the North-Western Sahara Aquifer System's groundwater resources using gravity data. *Journal of African Earth Sciences*, *178*, 104188. https://doi.org/10.1016/j.jafrearsci.2021.104188

Mohamed, A., Sultan, M., Ahmed, M., Yan, E., & Ahmed, E. (2017). Aquifer recharge, depletion, and connectivity: Inferences from GRACE, land surface models, and geochemical and geophysical data. *GSA Bulletin*, *129*(5–6), 534–546. https://doi.org/10.1130/B31460.1

Nakata, K., Hasegawa, T., Iwatsuki, T., & Kato, T. (2016). Comparison of ^{14}C collected by precipitation and gas-strip methods for dating groundwater. *Radiocarbon*, *58*(3), 491–503. https://doi.org/10.1017/RDC.2016.22

Newman, B. D., Osenbrück, K., Aeschbach-Hertig, W., Solomon, D. K., Cook, P., Rózański, K., & Kipfer, R. (2010). Dating of "young" groundwaters using environmental tracers: Advantages, applications, and research needs. *Isotopes in Environmental and Health Studies*, *46*(3), 259–278. https://doi.org/10.1080/10256016.2010.514339

Nicholson, S. (2000). The nature of rainfall variability over Africa on time scales of decades to millenia. *Global and Planetary Change*, *26*(1–3), 137–158. https://doi.org/10.1016/S0921-8181(00)00040-0

Observatoire du Sahara et du Sahel (OSS). (2002). *Une conscience de bassin: Hydrogéologie. Rapport interne. Coupes. Planches. Annexes*. Observatoire du Sahara et du Sahel.

Observatoire du Sahara et du Sahel (OSS). (2003). *Système Aquifère du Sahara Septentrional. Volume 2: Hydrogéologie. Projet sass Rapport interne. Coupes. Planches. Annexes*. Observatoire du Sahara et du Sahel.

Observatoire du Sahara et du Sahel (OSS). (2006). *Etude hydrogéologique du Système Aquifère de la Djeffara tuniso-libyenne. Rapport interne. Coupes. Planches. Annexes*. Observatoire du Sahara et du Sahel.

Pausata, F. S. R., Gaetani, M., Messori, G., Berg, A., Maia de Souza, D., Sage, R. F., & deMenocal, P. B. (2020). The greening of the Sahara: Past changes and future implications. *One Earth*, *2*(3), 235–250. https://doi.org/10.1016/j.oneear.2020.03.002

Pausata, F. S. R., Messori, G., & Zhang, Q. (2016). Impacts of dust reduction on the northward expansion of the African monsoon during the Green Sahara period. *Earth and Planetary Science Letters*, *434*, 298–307. https://doi.org/10.1016/j.epsl.2015.11.049

Petersen, J. O. (2014). *Traçage isotopique (36Cl, 4He, 234U) et modélisation hydrogéologique du Système Aquifère du Sahara Septentrional. Application à la recharge Quaternaire du Continental Intercalaire (These de doctorat)*. Aix-Marseille Université. Retrieved from http://www.theses.fr/fr/2014AIXM4325

Petersen, J. O., Deschamps, P., Gonçalvès, J., Hamelin, B., Michelot, J. L., Guendouz, A., & Zouari, K. (2014). Quantifying paleorecharge in the Continental Intercalaire (CI) aquifer by a Monte-Carlo inversion approach of ^{36}Cl/Cl data. *Applied Geochemistry*, *50*, 209–221. https://doi.org/10.1016/j.apgeochem.2014.04.014

Petersen, J. O., Deschamps, P., Hamelin, B., Fourré, E., Gonçalvès, J., Zouari, K., et al. (2018). Groundwater flowpaths and residence times inferred by ^{14}C, ^{36}Cl and ^{4}He isotopes in the Continental Intercalaire aquifer (North-Western Africa). *Journal of Hydrology*, *560*, 11–23. https://doi.org/10.1016/j.jhydrol.2018.03.003

Peyron, O., Jolly, D., Braconnot, P., Bonnefille, R., Guiot, J., Wirrmann, D., & Chalié, F. (2006). Quantitative reconstructions of annual rainfall in Africa 6000 years ago: Model-data comparison. *Journal of Geophysical Research: Atmospheres*, *111*(D24). https://doi.org/10.1029/2006JD007396

Pizzi, G., & Sartori, L. (1984). Interconnected groundwater systems simulation (IGROSS)—Description of the system and a case history application. *Journal of Hydrology*, *75*, 255–285. https://doi.org/10.1016/0022-1694(84)90053-2

Rightmire, C. T., & Hanshaw, B. B. (1973). Relationship between the carbon isotope composition of soil CO_2 and dissolved carbonate species in groundwater. *Water Resources Research*, *9*(4), 958–967. https://doi.org/10.1029/WR009i004p00958

Rogerson, M., Dublyansky, Y., Hoffmann, D. L., Luetscher, M., Töchterle, P., & Spötl, C. (2019). Enhanced Mediterranean water cycle explains increased humidity during MIS 3 in North Africa. *Climate of the Past*, *15*(5), 1757–1769. https://doi.org/10.5194/cp-15-1757-2019

Rousseau-Gueutin, P., Love, A. J., Vasseur, G., Robinson, N. I., Simmons, C. T., & de Marsily, G. (2013). Time to reach near-steady state in large aquifers. *Water Resources Research*, *49*(10), 6893–6908. https://doi.org/10.1002/wrcr.20534

Samborska, K., Różkowski, A., & Małoszewski, P. (2013). Estimation of groundwater residence time using environmental radioisotopes (^{14}C,T) in carbonate aquifers, southern Poland. *Isotopes in Environmental and Health Studies*, *49*(1), 73–97. https://doi.org/10.1080/10256016.2012.677041

Sanford, W. (2002). Recharge and groundwater models: An overview. *Hydrogeology Journal*, *10*(1), 110–120. https://doi.org/10.1007/s10040-001-0173-5

Scanlon, B. R. (2000). Uncertainties in estimating water fluxes and residence times using environmental tracers in an arid unsaturated zone. *Water Resources Research*, *36*(2), 395–409. https://doi.org/10.1029/1999WR900240

Scanlon, B. R., Healy, R. W., & Cook, P. G. (2002). Choosing appropriate techniques for quantifying groundwater recharge. *Hydrogeology Journal*, *10*(1), 18–39. https://doi.org/10.1007/s10040-001-0176-2

Scanlon, B. R., Keese, K. E., Flint, A. L., Flint, L. E., Gaye, C. B., Edmunds, W. M., & Simmers, I. (2006). Global synthesis of groundwater recharge in semiarid and arid regions. *Hydrological Processes*, *20*(15), 3335–3370. https://doi.org/10.1002/hyp.6335

Schulz, S., Horovitz, M., Rausch, R., Michelsen, N., Mallast, U., Köhne, M., et al. (2015). Groundwater evaporation from salt pans: Examples from the eastern Arabian Peninsula. *Journal of Hydrology*, *531*, 792–801. https://doi.org/10.1016/j.jhydrol.2015.10.048

Schulz, S., Walther, M., Michelsen, N., Rausch, R., Dirks, H., Al-Saud, M., et al. (2017). Improving large-scale groundwater models by considering fossil gradients. *Advances in Water Resources*, *103*, 32–43. https://doi.org/10.1016/j.advwatres.2017.02.010

Shanahan, T. M., McKay, N. P., Hughen, K. A., Overpeck, J. T., Otto-Bliesner, B., Heil, C. W., et al. (2015). The time-transgressive termination of the African Humid Period. *Nature Geoscience*, *8*(2), 140–144. https://doi.org/10.1038/ngeo2329

Skonieczny, C., Paillou, P., Bory, A., Bayon, G., Biscara, L., Crosta, X., et al. (2015). African humid periods triggered the reactivation of a large river system in Western Sahara. *Nature Communications*, *6*(1), 8751. https://doi.org/10.1038/ncomms9751

Srdoč, D., Obelić, B., Horvatinčić, N., Sliepčević, A., Stichler, W., Moser, H., & Geyh, M. A. (1982). Isotope analyses of groundwaters of the North African Plain. *Catena*, *9*(1), 253–263. https://doi.org/10.1016/S0341-8162(82)80017-910.1016/0341-8162(82)90004-2

Swezey, C. S. (1999). The lifespan of the complexe terminal aquifer, Algerian-Tunisian Sahara. *Journal of African Earth Sciences*, *28*(3), 751–756. https://doi.org/10.1016/S0899-5362(99)00043-3

Tierney, J. E., Pausata, F. S. R., & deMenocal, P. B. (2017). Rainfall regimes of the Green Sahara. *Science Advances*, *3*(1), e1601503. https://doi.org/10.1126/sciadv.1601503

Tjallingii, R., Claussen, M., Stuut, J.-B. W., Fohlmeister, J., Jahn, A., Bickert, T., et al. (2008). Coherent high- and low-latitude control of the northwest African hydrological balance. *Nature Geoscience*, *1*(10), 670–675. https://doi.org/10.1038/ngeo289

Trabelsi, R., Kacem, A., Zouari, K., & Rozanski, K. (2009). Quantifying regional groundwater flow between Continental Intercalaire and Djeffara aquifers in southern Tunisia using isotope methods. *Environmental Geology*, *58*(1), 171–183. https://doi.org/10.1007/s00254-008-1503-x

Tweed, S., Leblanc, M., Cartwright, I., Favreau, G., & Leduc, C. (2011). Arid zone groundwater recharge and salinisation processes; an example from the Lake Eyre Basin, Australia. *Journal of Hydrology*, *408*(3), 257–275. https://doi.org/10.1016/j.jhydrol.2011.08.008

Tzedakis, P. C. (2007). Seven ambiguities in the Mediterranean palaeoenvironmental narrative. *Quaternary Science Reviews*, *26*(17), 2042–2066. https://doi.org/10.1016/j.quascirev.2007.03.014

Verhagen, B. T. (1992). *Detailed geohydrology with environmental isotopes: A case study at Serowe, Botswana. Isotope techniques in water resources development 1991*. Retrieved from http://inis.iaea.org/Search/search.aspx?orig_q=RN:23034816

Vogel, J. C. (1967). Investigation of groundwater flow with radiocarbon. *Isotopes in Hydrology*.

Wood, C., Cook, P. G., & Harrington, G. A. (2015). Vertical carbon-14 profiles for resolving spatial variability in recharge in arid environments. *Journal of Hydrology*, *520*, 134–142. https://doi.org/10.1016/j.jhydrol.2014.11.044

Wood, C., Cook, P. G., Harrington, G. A., & Knapton, A. (2017). Constraining spatial variability in recharge and discharge in an arid environment through modeling carbon-14 with improved boundary conditions. *Water Resources Research*, *53*(1), 142–157. https://doi.org/10.1002/2015WR018424

Yermani, M., Chkir, N., Zouari, K., Michelot, J. L., Moumni, L., & de Biologie-Géologie, D. (2009). Environmental tracers as indicators of water fluxes through the unsaturated zone in Semiarid regions: The case of Gafsa plain (Southern Tunisia). *Journal of Environmental Hydrology*, *17*.

Yokochi, R., Bernier, R., Purtschert, R., Zappala, J. C., Yechieli, Y., Adar, E., et al. (2018). Field Degassing as a New Sampling Method for ^{14}C Analyses in Old Groundwater. *Radiocarbon*, *60*(1), 349–366. https://doi.org/10.1017/RDC.2017.64

Zammouri, M., & Ribeiro, L. (2017). Analyzing the effect of transmissivity uncertainty on the reliability of a model of the northwestern Sahara aquifer system. *Journal of African Earth Sciences*, *129*, 910–922. https://doi.org/10.1016/j.jafrearsci.2017.02.034

Zinn, B. A., & Konikow, L. F. (2007). Effects of intraborehole flow on groundwater age distribution. *Hydrogeology Journal*, *15*(4), 633–643. https://doi.org/10.1007/s10040-006-0139-8

Zouari, K., Trabelsi, R., & Chkir, N. (2011). Using geochemical indicators to investigate groundwater mixing and residence time in the aquifer system of Djeffara of Medenine (southeastern Tunisia). *Hydrogeology Journal*, *19*(1), 209–219. https://doi.org/10.1007/s10040-010-0673-2